Idealized Modeling of Convective Organization in a Changing Climate Using Multiple Equilibria in Weak Temperature Gradient Simulations

Stipo Sentić[1], and Sharon L. Sessions[1]

Corresponding author: S. Sentić, Physics Department and Geophysical Research Center, New Mexico Institute of Mining and Technology, 801 Leroy Place, Socorro, NM 87801, USA. (stipo.sentic@student.nmt.edu)

[1]Physics Department and Geophysical Research Center, New Mexico Institute of Mining and Technology, 801 Leroy Place, Socorro, NM 87801, USA.

Abstract.

Tropical convective organization is a process in which disorganized, scattered, convection organizes in a intensely precipitating region surrounded by dry, non-precipitating, regions. Convective organization regulates the atmospheric energy budget, and modulates the strength of severe and intraseasonal weather (e.g. hurricanes and the Madden-Julian Oscillation); understanding convective organization in a changing climate can help us better predict weather and climate.

To study tropical convective organization, we use a cloud resolving model in weak temperature gradient (WTG) mode, which effectively parameterizes the influence of the large-scale environment on local convection. We use radiative convective equilibrium simulations at different sea surface temperatures (SSTs) as a proxy for a changing climate and reference large-scale environments for the WTG simulations.

We find that the WTG multiple equilibria in precipitation, defined as wind speeds supporting both a precipitating and a non-precipitating steady state, resemble the precipitating and dry regions in organized convection. Compared to the present climate state, colder thermodynamic environments support a narrower range of multiple equilibria at higher wind speeds, and radiatively driven cold pool formation which was shown to influence convective organization at low SSTs. In contrast, at high SSTs, a narrower range of multiple equilibria exists at low wind speeds, which suggests increased prevalence of organized convection in a warming climate.

Furthermore, the change in diagnostic relationships between precipitation rate, atmospheric stability, moisture content, and large-scale transport of energy and moisture, with increasing SSTs shows more intense convection in precipitating regions of organized convection.

Three key point statements (140 character limit each):

Thermodynamic environments of cold climates support radiatively driven cold pool convective organization.

In warm climates, convective organization occurs at lower wind speeds compared to cold climates.

Convective diagnostics show strengthening of convection in warmer climates in precipitating regions of organized convection.

1. Introduction

Organization of tropical convection plays a critical role in weather and climate. Organized convection cools the atmosphere [*Bretherton et al.*, 2005; *Wing and Emanuel*, 2013; *Muller and Held*, 2012; *Tobin et al.*, 2012]—with more outgoing long-wave radiation, lower albedo, and fewer clouds—while disorganized convection warms it. Convection is known to organize and to initiate tropical cyclogenesis under forcing by disturbances such as Easterly waves [*Thorncroft and Hodges*, 2001], Kelvin waves, and the Madden Julian Oscillation [MJO, *Schreck III*, 2015]. However, recent numerical results [*Bretherton et al.*, 2005; *Muller and Held*, 2012; *Wing and Emanuel*, 2013] suggest that convective organization might occur without an apparent external forcing; radiative convective equilibrium (RCE) simulations spontaneously form organized regions of convection surrounded by dry regions—colloquially referred to as "self-aggregation". This spontaneous convective organization is strongly supported by higher sea surface temperatures [SSTs, *Wing and Emanuel*, 2013; *Coppin and Bony*, 2015]. Understanding spontaneous convective organization in the context of a changing climate can help in better predicting thermodynamic budgets and future climate states.

Recent advances in modeling tropical convection offer tools for studying convective organization in a changing climate in an idealized manner. One such tool is the weak temperature gradient (WTG) approximation [*Sobel and Bretherton*, 2000; *Raymond and Zeng*, 2005; *Herman and Raymond*, 2014]. Based on the observed weak horizontal temperature gradients in the tropics, the WTG approximation effectively parameterizes the large-scale in limited domain simulations, and it is used to study the the effects of changes in the large-scale temperature and moisture on local convection [*Sobel and Bretherton*, 2000; *Raymond and Zeng*, 2005; *Raymond and Sessions*, 2007; *Sessions et al.*, 2015, 2016]. Additionally, the WTG approximation allows for decoupling of dynamic and thermodynamic forcing to study their isolated effects on convection; researchers have studied the convective response to radiation [*Anber et al.*, 2014, 2015; *Wang et al.*, 2013, 2015; *Sessions et al.*, 2016], moisture treatment [*Wang and Sobel*, 2012; *Sessions et al.*, 2015], surface fluxes [*Raymond and Zeng*, 2005; *Sessions et al.*, 2010; *Anber et al.*, 2015], vertical wind shear [*Anber et al.*, 2014, 2015], sea surface temperatures [*Sobel and Bretherton*, 2000; *Wang and Sobel*, 2011; *Daleu et al.*, 2015], and changes in atmospheric stability and moisture [*Raymond and Sessions*, 2007; *Sessions et al.*, 2015, 2016]. The WTG approximation has also been applied to modeling the evolution of the thermodynamic environment in tropical cyclogenesis [*Raymond and Sessions*, 2007] and the Madden Julian Oscillation [*Wang et al.*, 2013, 2015; *Sentic et al.*, 2015], both known instances of convective organization.

The WTG approximation can be used for studying convective organization by utilizing the hypothesized analogy [*Anber et al.*, 2014; *Sessions et al.*, 2015, 2016] between the moist and dry regions in domains with organized convection and multiple equilibria in precipitation exhibited in WTG simulations [*Raymond and Zeng*, 2005; *Sessions et al.*, 2010; *Anber et al.*, 2014; *Herman and Raymond*, 2014; *Sessions et al.*, 2015, 2016]. Multiple equilibria in precipitation are defined as a dry or moist steady state for given boundary conditions when the domain is initialized dry or moist [e.g., *Sobel et al.*, 2007; *Sessions et al.*, 2010]. In this paper we study the SST dependence of multiple equilibria in precipitation in WTG simulations, to assess how the changing thermodynamic environment and dynamical forcing might support mechanisms controlling convective organization.

Studies of RCE simulations in cloud resolving models [CRMs, *Bretherton et al.*, 2005; *Posselt et al.*, 2012; *Muller and Held*, 2012; *Khairoutdinov and Emanuel*, 2013; *Wing and Emanuel*, 2013] and in a general circulation model [GCM, *Coppin and Bony*, 2015] have suggested mechanisms controlling tropical convective organization. Those mechanisms range from radiative forcing [*Wing and Emanuel*, 2013; *Coppin and Bony*, 2015], surface forcing [*Coppin and Bony*, 2015], and feedbacks between clouds, radiation, and moisture [*Wing and Emanuel*, 2013; *Emanuel et al.*, 2014; *Muller and Held*, 2012]. Recent investigations of RCE simulations and convective organization in a changing climate [*Posselt et al.*, 2012; *Coppin and Bony*, 2015] reveal that there are possibly two distinct mechanisms [*Coppin and Bony*, 2015] that govern cool (around 290 K) and warm (around 310 K) SSTs, with a more complex behavior in the intermediate range of SSTs (around 301 K). At cool SSTs, the organization occurs as a consequence of radiatively driven cold pools expanding in the boundary layer [*Muller and Held*, 2012; *Wing and Emanuel*, 2013; *Coppin and Bony*, 2015]. At warm SSTs, organization is heavily influenced by wind induced surface heat exchange [WISHE, *Coppin and Bony*, 2015] with convectively organized regions expanding outwards into dry regions. At intermediate SSTs, a mixture of the two mechanics occurs to exhibit critical behavior around 301 K [*Posselt et al.*, 2012; *Emanuel et al.*, 2014]. We will argue, in our qualitative comparison of WTG multiple equilibria to spontaneously organized convection, that the changing large-scale thermodynamic environment influences the mechanism of cold pool formation at low, intermediate, and high SSTs.

Previous studies (see above) focused on mechanisms of initiation and maintenance of organized tropical convection; here we focus on how diagnostics relevant to convective organization change with SST in our WTG simulations. Specifically, we study relationships among thermodynamic and dynamic diagnostics—e.g., wind speed, SSTs, precipitation rate, moisture content, stability, and large-scale transport—shown to be significant in tropical weather dynamics and convection [*Bretherton et al.*, 2004; *Masunaga*, 2012; *Raymond and Sessions*, 2007; *Gjorgjievska and Raymond*, 2014; *Sessions et al.*, 2015; *Sentic et al.*, 2015; *Sessions et al.*, 2016]. For example, studies found a strong connection between precipitation rate and column moisture content [*Raymond et al.*, 2003; *Bretherton et al.*, 2004; *Peters and Neelin*, 2006; *Raymond et al.*, 2007; *Neelin et al.*, 2009; *Masunaga*, 2012; *Sessions et al.*, 2015; *Sentic et al.*, 2015], precipitation rate and atmospheric stability [*Raymond and Sessions*, 2007; *Gjorgjievska and Raymond*, 2014; *Inoue and Back*, 2015a; *Sentic et al.*, 2015], between large-scale transport and precipitation rate, atmospheric stability, and column moisture content [*Inoue and Back*, 2015a; *Sessions et al.*, 2015; *Sentic et al.*, 2015], and between saturation fraction and instability index [*Sessions et al.*, 2015; *Sentic et al.*, 2015]. The relationships between these diagnostics [*Inoue and Back*, 2015b; *Sentic et al.*, 2015] are useful for studying convective organization in the context of the WTG approximation, and are able to differentiate organized from disorganized convection. Understanding how these relationships change in a changing climate can give us further insight into how convective organization might change.

This paper is organized as follows. In section 2 we describe the cloud resolving model, the WTG approximation, the diagnostic variables, and the methodology used in this study. In section 3 we describe the RCE simulations used in obtaining reference profiles for the WTG simulations, while in section 4 we examine multiple equilibria in precipitation in WTG simulations. Section 5 shows the diagnostic relationships in WTG multiple equilibria simulations. Sections 6 and 7 are the discussion and summary of our results, respectively.

2. Model and methodology

2.1. Cloud resolving model and the weak temperature gradient approximation

A full description of the cloud resolving model we use can be found in *Herman and Raymond* [2014]; *Sessions et al.* [2015]; *Sentic et al.* [2015]. The model solves in tandem the fully non-hydrostatic Navier-Stokes equations, the total water vapor mixing ratio, and the entropy equation (entropy being related to the equivalent potential temperature). The model achieves radiative convective equilibrium (RCE) in the absence of interactions with the large-scale environment. To parameterize large-scale environments on local convection we use the relaxed spectral weak temperature gradient (WTG) approximation.

The WTG approximation is based on the assumption that gravity waves redistribute heating anomalies that arise due to diabatic heating [*Bretherton and Smolarkiewicz*, 1989]. The redistributed energy causes adiabatic lifting of surrounding parcels via the vertical WTG mass transfer ρw_{WTG}. The WTG vertical velocity is given by:

$$w_{WTG}(z,t) = \sum_j \frac{\Theta_j(t)}{\tau_j} \sin(m_j z), \tag{1}$$

where $m_j = j\pi/h$ ($j = 1, 2, 3, ...$) are the vertical gravity wave wave-numbers, τ_j are the relaxation time scales for the vertical gravity wave modes, and $\Theta_j(t)$ are the Fourier coefficients which decompose the scaled potential temperature anomaly, $D_\theta(z,t)$, as:

$$\Theta_j(t) = \frac{2}{h} \int_0^h D_\theta(z,t) \sin(m_j z) dz. \tag{2}$$

Here, h is the tropopause height, and:

$$D_\theta(z,t) = \frac{\bar{\theta} - \theta_{ref}}{d\bar{\theta}/dz}, \tag{3}$$

where $\bar{\theta}$ is the model domain averaged potential temperature, θ_{ref} is the reference potential temperature, and $D_\theta(z,t)$ can be interpreted as the height a parcel needs to reach to remove a heating anomaly. The relaxation time scales τ_j relate to the horizontal length over which gravity waves dissipate heating anomalies as $\tau_j = Lm_j/N = \pi Lj/hN$, where N is the Brunt-Väisälä frequency. In this study, we used $\tau_1 = 1$ h for the base vertical wave-number, which corresponds to $L = 171.8$ km. The WTG vertical velocity is applied to the thermodynamic and total water vapor mixing ratio equations through which the model communicates with the reference environment. Please see *Herman and Raymond* [2014]; *Sessions et al.* [2015]; *Sentic et al.* [2015] for technical details of the implementation of the WTG approximation in the CRM.

We use the interactive simplified radiative cooling parameterization of *Raymond* [2001], where water vapor is used as the only active species in the radiative transfer model. The radiation scheme compares well qualitatively to the rapid radiative transfer model (RRTM) radiation package [*Mlawer et al.*, 1997] over the range of SSTs used in this study (not shown). Research shows that interactive radiation is conducive and in many models necessary to produce convective organization [*Muller and Held*, 2012; *Emanuel et al.*, 2014; *Sessions et al.*, 2016], and that WTG experiments using static radiative profiles hinder organization [*Sessions et al.*, 2016]. Our choice of interactive radiation is based on *Sessions et al.* [2016], who showed that interactive radiative cooling produces a larger range of multiple equilibria in WTG simulations.

Changes in the climate are parameterized via changes in SSTs, and consequently in changes in surface fluxes. We use a bulk surface entropy flux parameterization:

$$S_{ss} = C_d U_e (s_{ss} - s(0))b, \tag{4}$$

$$S_{rs} = C_d U_e (r_{ss} - r_t(0))b, \tag{5}$$

where S_{ss} and S_{rs} are the bulk surface sources of entropy and total water vapor mixing ratio, respectively, C_d is the transfer coefficient, $U_e = (u(0)^2 + v(0)^2 + W^2)^{1/2}$ is the effective surface wind speed with $W = 3$ m s^{-1} being the gustiness parameter, s_{ss} and r_{ss} are the saturated sea surface entropy and total water vapor mixing ratio, respectively, and $s(0)$ and $r_t(0)$ are the surface entropy and total water vapor mixing ratio, respectively. The coefficient $b = 2/\delta z$ corresponds to depositing the surface fluxes into a layer of $\delta z/2$ thickness, where δz is the model vertical grid spacing.

Sessions et al. [2015] showed that laterally entraining moisture by enforcing mass continuity in the WTG vertical velocity extends the range of multiple equilibria in precipitation in WTG simulations. Because we are interested in how the range of multiple equilibria changes in a changing climate, we use lateral entrainment to parameterize the effect of environmental moisture on the modeled convection.

We use two-dimensional model domains; *Wang and Sobel* [2011] showed that compared to three-dimensional simulations, two-dimensional simulations are warmer and and moister. Since our work is focused on qualitative comparison with current research, this should not be a deterrent. Also, since we are using small two-dimensional domains in our simulations, the RCE simulations used to produce reference profiles cannot self-aggregate as in other studies of organization of convection [e.g., as in *Wing and Emanuel*, 2013].

2.2. Diagnostic variables and relationships

In this paper, we are investigating how the dry and moist equilibrium states in precipitation can be used to study convective organization in a changing climate. We do this by relating diagnostics from our model to mechanisms that have been proposed in other research. We divide the diagnostics (defined below) in this study into two categories:

1. moisture related variables: precipitation rate, precipitable water, saturation fraction, and surface moist entropy fluxes,

2. temperature and large scale transport related variables: instability index, radiative cooling, deep convective inhibition (DCIN), and gross moist stability (GMS).

We study these diagnostics as a function of sea surface temperature (SST) and horizontal wind speed (without shear). Note that different SSTs have a significant impact on the reference environment (potential temperature and mixing ratio profiles, see methodology section below), so that surface entropy fluxes do not just reflect surface flux changes with changing SSTs, but also changing reference environments. Finally, we will study how diagnostic relationships relevant to tropical dynamics change in a changing climate.

Precipitation rate is a direct measure of convective activity, and is used to directly diagnose the dry and moist equilibrium states. To quantify moisture content, we consider both the precipitable water (vertically integrated mixing ratio), and saturation fraction (precipitable water divided by saturated precipitable water). Changes in precipitation rate (see section 5) are related to changes in precipitable water [*Bretherton et al.*, 2004; *Peters and Neelin*, 2006]. Several studies have found an increase in precipitation rate with increasing saturation fraction [*Bretherton et al.*, 2004; *Peters and Neelin*, 2006; *Raymond*, 2007]. We are interested how this relationship changes in a changing climate.

Instability index is a temperature dependent diagnostic defined as the difference between the average saturated moist entropy between 1 and 3 km and 5 and 7 km; a lower instability index corresponds to a more stable atmosphere. WTG simulations of the tropical atmosphere [*Raymond and Sessions*, 2007; *Raymond and Flores*, 2016] and observations [*Gjorgjievska and Raymond*, 2014; *Sentic et al.*, 2015; *Raymond and Flores*, 2016] have shown that a decrease in the instability index results in a bottom heavy mass flux profile which concentrates moisture convergence at lowest, moistest, levels, which increases saturation fraction and therefore precipitation rate [*Raymond and Sessions*, 2007; *Sessions et al.*, 2015; *Sentic et al.*, 2015]. This mechanism is hypothesized to play a role in convective organization [*Gjorgjievska and Raymond*, 2014; *Raymond et al.*, 2014; *Sessions et al.*, 2015; *Sentic et al.*, 2015].

Radiative cooling is defined here as the vertical integral of the model radiative cooling, while deep convective inhibition (DCIN) is defined as:

$$DCIN = s_t^* - s_b, \tag{6}$$

where s_t^* is the saturated moist entropy averaged from 1750 to 2000 m, and s_b is the moist entropy averaged from 0 to 750 m. Increased DCIN suppresses convection, while low DCIN is conducive to the development of convection. *Sessions et al.* [2016] demonstrated the importance of DCIN in the dry equilibrium, which we will also show in this paper.

Finally, the gross moist stability (GMS) quantifies the large scale transport between the local convection and the environment. GMS is defined as [e.g., *Raymond et al.*, 2009]:

$$GMS = -\frac{\langle \vec{\nabla} \cdot (s\vec{v}) \rangle}{\langle \vec{\nabla} \cdot (r_t\vec{v}) \rangle}, \tag{7}$$

where s is the moist entropy, and $\vec{v}$ is the horizontal wind speed; the brackets denote a horizontal and vertical average. In other words, GMS is moist entropy export divided by moist entropy import. A number of recent studies have used GMS as a measure of convective activity in numerical simulations [*Sobel et al.*, 2014; *Sessions et al.*, 2015, 2016; *Inoue and Back*, 2015a; *Sentic et al.*, 2015], and in observations [*Inoue and Back*, 2015a; *Sentic et al.*, 2015]. Negative GMS values correspond to situations where both entropy and moisture are exported, while positive GMS values correspond to situations where either entropy is imported and moisture is exported, or vice versa. In this study we exclude values of GMS for which the denominator exceeds one tenth of the numerator to avoid division by zero which makes the GMS vary widely at transitions from moisture export to moisture import and vice versa.

2.3. Methodology

In order to generate reference environments to represent the large-scale environment, we first run the model (the domain is 200 and 20 km in the horizontal and vertical, respectively; horizontal and vertical resolutions are 1 and 0.25 km, respectively) in a non-WTG mode for 150 days to a RCE state. We do this for eleven SST values (290, 292, 295, 299, 300, 301, 302, 303, 305, 307, and 310 K), and with a horizontal wind speed of 5 m s^{-1}. The last 30 days of the RCE simulations are averaged to provide the reference temperature and total mixing ratio profiles for the WTG simulations. For each SST, we perform WTG simulations using RCE profiles with the same SST. Each set of WTG simulations (using a different SST and corresponding reference environment) included horizontal wind speeds ranging from 0 to 20 m s^{-1} (see figure 4 for the choice of wind speed values for each SST). We also perform WTG simulations for a wind speed of 70 m s^{-1} (corresponding to a category 5 hurricane), to observe the asymptotic behavior of the diagnostic relationships studied in this paper.

For each WTG simulation we perform a pair of simulations in which the model is initialized either dry or moist. For a given wind speed and SST, if a dry initialized simulation stays dry while a moist initialized sustains precipitating equilibria, than those conditions support multiple equilibria. If a dry initialized simulation eventually precipitates (or a moist one drys out) a single equilibrium state is reached. The dry and moist initialized simulations are run for 90 and 45 days, respectively, as in [*Sessions et al.*, 2010]. Diagnostic quantities are calculated and averaged over the last 30 days of the WTG multiple equilibrium simulations.

3. Radiative convective equilibrium

RCE simulations are used to generate reference profiles of potential temperature and mixing ratio for WTG simulations. In this work, reference profiles from RCE simulations are obtained by running the CRM with WTG turned off. The RCE simulations are performed for SSTs ranging from 290 to 310 K—as a proxy for different climates—and wind speed of 5 m s^{-1} (see section 2 for details). We first characterize the reference environments for all climates ranging from 290 K to 310 K SST. Since we are interested in understanding diagnostic relationships and how they change with a warming environment, we analyze diagnostics of the RCE and how these change in warming, as a base for comparisons with WTG multiple equilibria in the next sections.

Figures 1a and 1b show profiles of potential temperature and mixing ratio for different SSTs; higher SSTs produce warmer and moister RCE steady states with the potential temperature increasing from about 300 K at a 10 km height for the 290 K SST RCE, to about 380 K at 10 km for the 310 K SST RCE profiles; surface mixing ratios increase from 8 g kg^{-1} to 30 g kg^{-1} going from 290 K SSTs to 310 K SSTs. Static stability decreases, implied by an increase in slope of the potential temperature from the surface to 7 km.

The warming and moistening anomalies, relative to the 300 K SST reference profiles, are shown in figures 1d and 1e. The potential temperature anomaly increases from about -27 K at 11 km with an SST of 290 K, to +40 K at 14 km for SST at 310 K. The moistening anomaly is greatest at the surface, but extends deep into the troposphere for warm SSTs (up to 14 km), while the drying anomaly only extends up to about 8 km for lower SSTs. The increase in the magnitude and height of the maximum precipitation mixing ratio, shown in figure 1c, suggests that latent heat release due to precipitation causes warming in ever higher levels (the maximum increases from values 0.1 g kg to 0.37 g kg, from height of 7 to about 13 km), accompanying an increase in altitude of the cloud base from about 2 to about 7 km. This might be a consequence of increase in height of the vertical velocity maximum. The scaling of the vertical velocity with increasing SSTs has been addressed in *Singh and O'Gorman* [2015]. The authors found that the square of the strongest updraft velocities scale with the vertically integrated buoyancy for increasing SSTs. Series of idealized plume models suggested that entrainment acted on the scaling of the vertical velocities via changes in the mean lapse rate with increasing SSTs. Radiative cooling, shown in figure 1f, balances the diabatic heating associated with convection; the level of maximum cooling, of -7 K, at a SST of 290 K is about 5 km, while the warmest SST (310 K) produces cooling of -10 K at 11 km.

RCE diagnostic relationships are shown in figure 2. The RCE precipitation rate grows with increasing SSTs from about 3 to about 5 mm day^{-1} (figure 2a). Since we impose constant insolation, energetics would have us expect a more constant RCE precipitation rate with increasing SST. However, since we fix greenhouse gas concentrations with SST, we do not account for greenhouse gas effects on radiative cooling which would make RCE precipitation rates more consistent with SST changes. Consequently, in our simulations we effectively decouple convective action in warming of the atmosphere, from warming due to greenhouse gas effects. We leave studying the effect of greenhouse gases on convective organization in a changing climate for future studies.

RCE precipitation rate increases with moistening (figure 2b); the RCE saturation fraction, which is a measure of moisture content, grows from 0.73 at cool SSTs to 0.85 at high SSTs (figure 2e). Note that a small increase in saturation fraction corresponds to a large increase in water vapor content in the troposphere (compare to figure 2b). The RCE precipitation rate also increases with the RCE instability index (figure 2c). The RCE atmospheric instability increases from about 2 J K^{-1} kg^{-1} at 290 K SST, to about 27 J K^{-1} kg^{-1}, with increasing SSTs (figure 2f). The RCE saturation fraction increases with decreasing stability (figure 2d). We will contrast this RCE relationship to results in conditions resembling organized convection below.

In the next section we study how local convection responds to changes in the RCE reference environment presented in this section. Specifically, we will analyze the non-precipitating and precipitating equilibrium states in light of organized convection and dry regions that surround it.

4. Multiple equilibria in precipitation

In this section, we study multiple equilibria in precipitation, defined as having both precipitating and non-precipitating steady states for given boundary conditions (i.e. reference potential temperature and mixing ratio profiles, and imposed wind speed), depending on whether the model is initialized dry or moist [*Sobel et al.*, 2007; *Sessions et al.*, 2010]. First we demonstrate the existence of multiple equilibria in our simulations, and relate that to the convective organization analogy. Next we diagnose the transition from the non-precipitating to the precipitating state in simulations which are initially dry but eventually develop persistent precipitation to better understand the transition to deep convection [*Peters and Neelin*, 2006]. Finally, we analyze vertical profiles of diagnostics for precipitating and non-precipitating simulations, and compare our results to studies on mechanisms of convective organization.

Multiple equilibria in precipitation can be seen in figure 3, which shows the precipitation rate versus horizontal wind speed for SSTs of 290, 300, 303, and 310 K, for simulations that are either initially dry (dotted lines, open symbols) or moist (solid lines and symbols). We notice that:

1. Higher SSTs support larger precipitation rates compared to lower SSTs.

2. The moist initialized runs precipitate over a broader range of wind speeds than the dry initialized runs.

3. The range of wind speeds that support multiple equilibria in precipitation—i.e., exhibiting both a precipitating and a non-precipitating steady state depending on initial moisture—differs for different SSTs. For example, at 290 K SST, the wind speeds that support multiple equilibria range from about 7 to 16 m s^{-1}, while an SST of 310 K only supports multiple equilibria from 0 to 6 m s^{-1}. The range of wind speeds that support a single non-precipitating state also varies with SSTs—at the SST of 290 K that range is from 0 to 7 m s^{-1}, while it does not exist for 310 K SST.

4. The wind speed where multiple equilibria transition to a single equilibrium, which we define as the critical wind speeds, varies with SST.

We can use these properties of the multiple equilibria to define an analogy between the multiple equilibria in precipitation and dry and precipitating regions in organized convection.

4.1. Multiple equilibria regions and organization analogy

Figure 3 showed that the critical wind speeds associated with the multiple-to-single equilibrium transition vary with SST; here, we investigate this over the entire range of SSTs. Figure 4 shows a phase diagram of precipitation as a function of horizontal wind speed and SSTs; dry initialized simulations are shown in figure 4a—with empty and solid symbols representing non-precipitating and precipitating steady states, respectively—while figure 4b shows the corresponding diagram for moist initialized simulations. Different colors correspond to different SSTs, while wind speed dependence is symbol coded, e.g. wind speeds of 2 m s^{-1} are denoted with a plus, while wind speeds of 20 m s^{-1} are shown in triangles pointing up. Figure 4 also serves as a color and symbol legend for figures 7, 8, 9, and 10.

Figure 4 also shows two curves: the solid and dashed curves present eye guides for the SST dependence of the critical wind speeds separating multiple equilibria from the single precipitating equilibrium, and multiple equilibria from the single non-precipitating equilibrium, respectively. These curves separate three regions:

1. A region of high wind speeds across all SSTs where a single precipitating equilibrium exists; we interpret this as conditions favoring less organized convection.

2. A region of intermediate wind speeds across all SSTs where multiple equilibria exist; we interpret this as a region of conditions favoring organized convection; under these conditions there exists the possibility for organized convective regions to be surrounded by dry non-precipitating regions.

3. A region of low wind speeds and low SSTs where a single non-precipitating equilibrium exists, where convection cannot form even in a moist environment. This region might strongly support conditions for radiatively driven cold pools, similar to the cold pool regions in *Coppin and Bony* [2015, see discussion section].

The region of organized convection (second point in the list above) where multiple equilibria exist shows an interesting pattern with climate change. At low SSTs, the region is narrow compared to the median 300 K SST, and exists for higher wind speeds. At high SSTs, this region is narrow but exists for low wind speeds. This pattern is reasonable in light of warmer and moister reference profiles at higher SSTs; the reference environment permits precipitation to occur at lower surface moist entropy forcing. However, the largest range of wind speeds supporting organized convection exists around 300 K SST, which is closest to the current climate state. This suggests that convective organization happens easier at low wind speeds, for higher SSTs, while any increase in surface fluxes beyond this region results in more widespread convection.

Examining the transition from dry to precipitating conditions can tell us which mechanisms affect the critical wind speed and range of multiple equilibria, and, consequently, convective organization. Next, we analyze the transition to precipitating conditions at the multiple-to-single equilibrium boundary.

4.2. Transition to a precipitating state

To better understand the existence of multiple equilibrium states for identical boundary conditions, we investigate how convection evolves in the transition from an initially dry state to a precipitating state. Figure 5 shows a time series of instability index, saturation fraction, and vertically averaged mass flux (a), and vertical profiles of mass flux (b), radiative cooling (c), and entropy (d) at days 2 (black), 6 (blue), 10 (red) and 18 (green) of the simulation at 303 K SST, and horizontal wind speed of 13 m s^{-1}, which is a case near the boundary of the multiple-to-single equilibrium transition (figure 4).

We first focus on the vertically averaged mass flux (figure 5a, black line) and vertical mass flux profiles (figure 5b). In general, subsidence occurs until about day 11, after which convection initiates and develops. At day 2 the mass flux is completely subsiding, and over days 2-11 develops a boundary layer circulation that moistens the boundary layer and the troposphere up to 3 km, which can be seen in the gradual increase in the saturation fraction (figure 5a, blue time series), and the increase in the moist entropy (figure 5d).

The radiation (figure 5c) shows strong cooling at low levels, especially in the boundary layer at day 2. Radiative cooling decreases in the boundary layer as the lower troposphere moistens during days 2–11, after which the radiation cools a deeper level and eventually exhibits strong warming in the boundary layer after the onset of convection. This pattern in radiation is ubiquitous across all the multiple equilibria simulations; simulations which remain dry exhibit strong cooling in and above the boundary layer [*Sessions et al.*, 2016], while precipitating simulations show strong cooling in the upper troposphere and warming in the boundary layer.

These results show that in precipitating simulations, the surface forcing overcomes the subsidence due to radiative cooling to produce conditions supporting convection, while in non-precipitating simulations the surface forcing is not sufficient. Now, we look how this forcing varies with SST and wind speed, and how that affects the range of multiple equilibria. Depending on SST and horizontal surface wind speed, these snapshots can exist in steady states, and these profiles result in specific diagnostic signatures which provide important clues about mechanisms of convective organization.

4.3. Vertical profiles of multiple equilibria diagnostics

A deeper comparison of our results to other research requires us to look at vertical profiles of diagnostic variables. First we look at the transition from multiple equilibria to a single precipitating equilibrium for the 300 K SST, as a function of wind speed, to show that the snapshots from figure 5 exist in steady states and that they can be used to characterize mechanisms of convective organization. Second, we look at how these diagnostic vertical profiles, and mechanisms, change with SST for the wind speed of 10 m s^{-1}. The results are similar for other wind speeds and SSTs (not shown).

Figure 6 shows vertical profiles of the potential temperature anomaly from the reference profile, the total water vapor mixing ratio anomaly from the reference profile, the radiative cooling, and the mass flux for non-precipitating and precipitating simulations for the 300 K SST, for wind speeds ranging from 2 m s^{-1} to 20 m s^{-1}. The non-precipitating simulations exhibit cooling at the top of the boundary layer (at about 1 km), and strong surface warming due to increasing surface entropy fluxes, with a negligible cooling in the troposphere (figure 6a). The boundary layer moisture increases with increasing wind speed (figure 6c), as a consequence of increasing surface entropy fluxes with wind speed; as the wind speed increases to the critical wind speed, the boundary layer moisture increases to RCE values (exhibited as a low mixing ratio anomaly). The non-precipitating simulation at the multiple equilibria-single equilibrium transition (with 16 m s^{-1} wind speed) is qualitatively different; there is a moistening above the boundary layer (figure 6c). This moistening is a consequence of the development of the boundary layer circulation explained in section 4.2; with increasing surface fluxes, the mass flux profile (figure 6g) goes from completely subsiding for wind speeds lower than 16 m s^{-1}, to developing an updraft above the surface and lifting the level of the subsidence maximum above the boundary layer for the wind speed of 16 m s^{-1}—this circulation moistens the boundary layer. Radiative cooling (figure 6e) also shows the impact of this circulation; there is a strong drying at the top of the boundary layer for simulations with wind speeds lower than 16 m s^{-1}, and an increase in the level of maximum cooling for the simulation at 16 m s^{-1}, which is a consequence of the moistening above the boundary layer.

The precipitating simulations, on the other hand, show a strong cooling in the boundary layer and at the surface (figure 6b), and a strong warming in the troposphere from 1 to 13 km (with a maximum at about 6 km), except for the 5 m s^{-1} wind speed simulation. Because the 5 m s^{-1} wind speed simulation is at the RCE forcing wind speed, convective events are intermittent, which influences the vertical profiles; at higher wind speeds convection is more continuous and produces stronger anomalies from the RCE state. The precipitating simulations also exhibit a dryer boundary layer, and a moister troposphere (figure 6d); the mixing ratio anomaly becomes more positive with increasing wind speeds. This is a consequence of increasing import of moisture from the lower levels, due to increase in the mass flux (figure 6h). Consequently, the radiative cooling decreases in the lower troposphere (figure 6f); and the surface fluxes warm the surface of the boundary layer.

The GMS in figure 6i summarizes the transition from multiple equilibria to a single equilibrium (precipitation rate is overlaid as a guide for the transition). For non-precipitating simulations the GMS decreases from 0.2 at 2 m s^{-1}, to approximately -0.4 at the transition wind speed of 16 m s^{-1}, while the dry initialized precipitating simulations (above 17 m s^{-1}) exhibit a positive GMS (around 0.4). The moist initialized precipitating simulations, show an increasing GMS from a small negative value at 5 m s^{-1}, to about 0.5 at 20 m s^{-1} surface wind speed. The difference between the GMS for the precipitating and non-precipitating simulations with increasing wind speeds shows how the the gradient of energy and moisture transport becomes more pronounced as we near the transition.

Figure 7 shows the same diagnostic profiles as in figure 6, but for a surface wind speed of 10 m s^{-1}, and SSTs ranging from 290 K to 310 K (see figure 4 for the color legend). Most of the the non-precipitating simulations show a strong cooling at the top of the boundary layer (figure 7a), similar to the transition simulation in figure 6a. The boundary layer mixing ratio anomaly is similar for all the SSTs (figure 7c); together with figure 6c this shows how the boundary layer moisture anomaly depends strictly on wind speed, while the tropospheric mixing ratio anomaly depends on SST, and consequently on the reference environment. Boundary layer radiative cooling is similar for all the SSTs (figure 7e), except for the SST near the transition to a precipitating state (305 K). In the troposphere, the radiative cooling increases with height for increasing SST as a consequence of a warming reference environment. Finally, the strongest subsidence at the top of the boundary layer occurs for lowest SSTs (figure 7g), with the depth of the subsidence layer increasing from

10 km at the 290 K SST, to 15 km at the 310 K SST. The 305 K SST mass flux profile exhibits the moistening circulation explained in section 4.2, while lower SSTs exhibit strict subsidence in the boundary layer.

The precipitating simulations show an increasing heating anomaly with increasing SST (figure 7b), note that the height of the heating maximum changes non-monotonically with SST. The heating anomaly maximum decreases from about 10 km for SSTs lower than 300 K, and increases from 5 to about 8 km from 300 to 310 K SST. Since the WTG vertical velocity is intimately linked with this heating anomaly, this behavior is reflected in the mass flux profiles (figure 7h); the height of the mass flux maximum also varies non-monotonically with SST. The strength of the tropospheric mixing ratio anomaly increases with SST, both in magnitude and height of the maximum (from about 2.5 km to 7 km), while the boundary layer anomaly remains negative as in precipitating simulations from figure 6d. While the radiative heating increases with SST at the surface, the radiative cooling decreases in the lower troposphere (from 1 to about 7 km) and increases in the higher troposphere (from about 7 km to 15 km).

Figure 7i shows how the GMS varies with SST for precipitating and non-precipitating simulations as a function of SST (precipitation rate is overlaid as a guide for the transition from multiple equilibria to a single equilibrium). For the non-precipitating simulations the GMS remains around -0.25 (with a local minimum around 300 K SST); the changes in the GMS for dry regions seem to be a weak function of the reference environment, and a stronger function of wind speed (figure 6i). In the precipitating simulations, on the other hand, GMS shows stronger variability with SST with an inflection point around 300 K

SST. The GMS decreases from 290 K to 295 K SST, increases from 295 K to 303 K SST, and again decreases from 303 K to 310 K SST.

These results show differences between precipitating and non-precipitating simulations. The non-precipitating simulations exhibit strong cooling at the top of the the boundary layer caused by radiatively driven subsidence, over the range of SSTs used in our study. This is similar to the radiatively driven cold pool mechanism of organization from *Coppin and Bony* [2015]. The precipitating simulations exhibit strong cold pools in the boundary layer (figure 7b), driven by convective downdrafts [figure 7h, boundary layer *Feng et al.*, 2015]. The significance of cold pools for convective organization has been addressed in previous studies [*Muller and Held*, 2012; *Jeevanjee and Romps*, 2013; *Coppin and Bony*, 2015; *Feng et al.*, 2015], and our results support their findings; radiatively driven cold pools prevent dry regions in initiating convection, and they export energy and moisture out of the domain. Furthermore, our results show how the moistening circulation in the boundary layer strengthens with increasing wind speeds to support conditions leading to convective initiation [see, e.g., *Muller and Held*, 2012].

To better understand changes in these mechanisms with changing SSTs and surface wind speeds, we now turn to diagnostic relationships.

5. Diagnostic relationships in WTG multiple equilibria simulations

The results from section 4 suggest that conditions over which convection organizes is sensitive to the climate state (here represented by SST). To better understand changes in convective organization in a changing climate, we analyze diagnostic relationships from the multiple equilibria experiments. Assuming the hypothesized analogy between dry and precipitating regions in organized convection and non-precipitating and precipitating equilibria in WTG simulations, we can investigate how organization might change in a warming environment.

We first focus on the dependence of the diagnostics on SSTs and wind speed. The natural inclination to look at bulk surface fluxes which combine the SST and wind speed influences is not straightforward because of the changes of reference profiles with SST; by changing SSTs we do not just change the surface fluxes but also the reference environment.

5.1. SST and horizontal wind speed dependence

Figures 8 and 9 show how the diagnostics depend on the SST (left column), and wind speed (right column). Figure 8 shows the dependence of precipitation rate, precipitable water, saturation fraction, and surface entropy fluxes. Figure 9 shows the dependence of instability index, radiative cooling, DCIN, and GMS. Figure 4 serves as a color and symbol legend for figures 8 and 9. The solid circle symbols with a black outline correspond to dry initialized simulations with a wind speed of 70 m s^{-1} (category 5 hurricane wind speed threshold); these were performed to study the asymptotic behavior of the convective diagnostics (e.g. see the instability index-SST relationship in figure 9a). Also, for comparison, the RCE values of precipitable water, saturation fraction, surface entropy fluxes, instability index, and radiative cooling are plotted as empty black boxes in figures 8c, 8e, 8g, 9a, and 9c. In this and the following sections we do not differentiate in which region from figure 4 the simulations belong to.

5.1.1. Precipitation and moisture related variables

The precipitation rate increases non-linearly with SST (e.g., by observing upward facing triangles in figure 8a) but approximately linearly with wind speed (e.g. observing the red symbols in figure 8b). For the same wind forcing, warmer climates support stronger precipitation rates. The non-linear behavior of precipitation rate with SST seems to be related to the amount of moisture that the troposphere can hold which can be seen in the precipitable water dependence on SST (figure 8c). Values of precipitable water in precipitating simulations are very close to the RCE values (shown with black squares in figure 8c). Also, figure 8d shows a weak dependence of the precipitable water on wind speed; the thermodynamic environment sets the limit on maximum moisture content of the troposphere. In other words, the maximum saturation fraction—which combines the effects of the domain temperature and moisture content—is limited by the reference environment, as seen in figures 8c–d.

Figure 8e shows the saturation fraction increasing with SST for all precipitating simulations. Interestingly, the saturation fraction for the precipitating simulations is greater than the RCE saturation fraction (empty black boxes in figure 8e), but lower than RCE for dry simulations. In large scale simulations of convective organization [*Bretherton et al.*, 2005; *Muller and Held*, 2012; *Wing and Emanuel*, 2013], the dry and precipitating regions exhibit a similar effect; regions of intense convection exhibit a larger saturation fraction than the average RCE value, while dry regions are much dryer compared to the RCE mean. Also, figure 8f shows that in precipitating simulations, the saturation fraction asymptotes to the maximum value with increasing wind speeds, for simulations having the same SST and reference profile (denoted by the same color). The dry simulations with wind speeds just below the critical wind speed marking the transition to a single precipitating equilibrium (see dashed line in figure 4a) shows a higher saturation fraction compared to dry runs at lower wind speeds, with a maximum near 301 K SST. This occurs because the circulation developing in the boundary layer moistens the boundary layers and the lowest levels of the troposphere (see section 4.2), but is not strong enough to overcome the subsidence and produce conditions leading to convection. Non-precipitating simulations at lower wind speeds do not exhibit this boundary layer circulation and have lower saturation fraction.

The surface entropy fluxes (figure 8g–h) help explain the pattern observed in the saturation fraction (figure 8e) for the dry equilibrium; a majority of the simulations have surface fluxes stronger than the RCE values (shown in black squares). Figure 8g shows the surface entropy fluxes as a function of SST; the dashed line is a guideline corresponding to the multiple equilibria-single precipitating equilibrium transition seen in figure 4a. The guideline identifies a critical surface entropy flux for each SST, above which dry-initialized simulations precipitate. The critical surface entropy fluxes exhibit a maximum near 301 K SST. This suggests that the non-monotonic dependence of the critical wind speed separating the multiple equilibria and the single precipitating equilibrium (figure 4a) is influenced by the critical surface entropy flux values. Since the critical surface entropy flux values depend on the SST—and consequently on the the reference profiles—so does the critical wind speed (see dashed line in figure 4). The precipitating simulations in figures 8g–h show a natural consequence of the bulk surface flux parameterization; they increase as wind speed and SSTs increase, where the latter also occurs because of the changes in the reference profiles with change of SSTs.

5.1.2. Temperature and radiation related variables; GMS

Previous research [*Raymond and Sessions*, 2007; *Gjorgjievska and Raymond*, 2014; *Raymond et al.*, 2014; *Sessions et al.*, 2015, 2016; *Sentic et al.*, 2015; *Raymond and Flores*, 2016] has identified a relationship between moisture and the instability index. Figure 2d showed that in RCE, a higher instability index is correlated with an increase in saturation fraction, and increased precipitation rates (figure 2c). Figures 9a–b show how the instability index depends on SST and wind speed in WTG simulations.

The RCE instability index (shown in black squares in figure 9a) increases monotonically with SST—the ever stronger warming of the troposphere decreases the mean static stability of the reference environment. The non-precipitating simulations remain close to the stability values of the RCE simulations with low SSTs having slightly weaker stability than the RCE, and high SSTs having stronger stability (lower instability index) than the RCE. The precipitating simulations, on the other hand, show significantly different behavior; at higher SSTs, the precipitating simulations are much more stable than the RCE. Note that the outlined bullets correspond to simulations with 70 m s^{-1} wind speeds (as a proxy for extreme values); they have the lowest values of instability index. The instability index associated with high wind speeds also exhibits a maximum near 301 K SSTs. This behavior is similar to the critical surface flux behavior for the dry simulations in figure 8g. Figure 9b shows that precipitating simulations, for a given SST, have a decreasing instability index for increasing wind speeds. This suggests that the increasing difference between the WTG and RCE instability index in the precipitating simulations for increasing SST (figure 9a) is in part due to the wind speed, while the asymptotic value of the instability index at a given SST, depends on the reference environment. To summarize, in a warming environment the differences in instability index between convectively active regions and non active regions might become more pronounced.

The vertically integrated radiative cooling—which is a proxy for outgoing longwave radiation (OLR)—and its dependence on the SST and the wind speed is shown in figures 9c–d.

The radiative cooling shows a difference between the precipitating and non-precipitating simulations characteristic of convective organization: non-precipitating simulations, corresponding to dry regions in organized convection, exhibit stronger cooling compared to the RCE mean, while precipitating simulations, corresponding to convecting regions in organized convection, cool less compared to the RCE mean. Radiative cooling increases with SSTs for the dry simulations (figure 9c), while for a given SST it varies little with wind speed (figure 9d). The precipitating simulations show a mild decrease in radiative cooling with increasing SST, except for the high wind speed simulations which show a weak decrease, and then a strong increase in radiative cooling for the 310 K SST. The latter behavior shows a qualitative change in convective behavior at higher SSTs. The wind speed dependence (figure 9d) shows that in precipitating simulations the radiative cooling is more constrained by changes in wind speed than by changes in SST (or, by implication, the reference environment). The strong SST dependence and wind speed constraint of radiative cooling in dry and precipitating simulations, respectively, indicates the relative importance of dynamics and thermodynamics in the dry and convective regions in organized convection.

DCIN (figures 9e–f) shows more variability for the non-precipitating than for the precipitating simulations. The precipitating simulations have a small DCIN, while the non-precipitating simulations show variation both in SST and wind speed. Increasing SSTs cause a strong increase in DCIN for the same wind speed. Increasing wind speeds (figure 9f) tends to decrease the spread in DCIN that is shown for different SSTs at lower wind speeds. This is a consequence of the increasing moisture content of the troposphere near and in the boundary layer (see section 4). This behavior suggests that DCIN may be important for characterizing the dry non-convecting regions of organized convection [see also *Sessions et al.*, 2016].

The GMS also shows an interesting separation between the non-precipitating and precipitating simulations (figures 9g, h); most of the dry simulations have negative GMS which increases in magnitude with increasing wind speeds (figure 9h), with the exception of the 2 m s^{-1} simulations. The 2 m s^{-1} non-precipitating simulations export moisture but import moist entropy, due to boundary layer circulations (not shown). We don't completely trust the GMS for wind speeds below the RCE forcing, because it could be a numerical artifact of a weakly resolved boundary layer in our model. In the non-precipitating simulations we see a strong dependence of the GMS on wind speed. In the precipitating simulations, on the other hand, for a given SST, the GMS decreases with increasing wind speed (figure 9g, or does not vary much in case of high SSTs); higher wind speeds asymptote the GMS towards a SST dependent characteristic value (see next section). SST dependence shows a decrease of GMS scatter towards smaller values, for higher SSTs (figure 9g). A small positive GMS corresponds to stronger import of moisture compared to export of moist entropy, which suggests more vigorous convection at higher SSTs. This GMS behavior correlates to the behavior of convection in other studies of organized convection [*Bretherton et al.*, 2005; *Muller and Held*, 2012; *Wing and Emanuel*, 2013]. In those studies, non-precipitating regions in organized convection export moisture and energy, while in precipitating regions, energy and moisture are imported. This correspondence suggests WTG multiple equilibria as a valuable analogue for studying convective organization in an idealized framework.

Next, we will look at how convective relationships change in a changing climate, and how those changes can influence convective organization.

5.2. Convective relationships

To better model convective organization and energy budgets, it is important to understand how convective diagnostics change in changing climate. Figure 10 shows precipitation rate as a function of saturation fraction, instability index, and GMS; saturation fraction versus instability index; saturation fraction versus GMS; and instability index versus GMS. Previous research has shown that these relationships hold valuable analogies for connecting the multiple equilibria to organized convection [*Sessions et al.*, 2015, 2016; *Sentic et al.*, 2015]. In figure 10, we will be showing only SSTs of 290, 295, 300, 303, 307, and 310 K, in order to more clearly see the relationships, and we will connect the precipitating simulations for a given SST with lines to serve as guidelines.

The relationship between precipitation rate and saturation fraction shows a well substantiated finding; higher saturation fraction leads to higher precipitation rates [*Bretherton et al.*, 2004; *Peters and Neelin*, 2006; *Gjorgjievska and Raymond*, 2014; *Sentic et al.*, 2015]. Non-precipitating simulations have lower saturation fraction compared to the precipitating simulations. However, precipitating simulations exhibit different asymptotic behavior in the relationship between precipitation rate and saturation fraction for different SSTs; higher SSTs support higher saturation fractions, which in turn support higher precipitation rates. The inset in figure 10a shows only the precipitating simulations, magnifying this relationship. These results suggest that the reference environment sets the characteristic asymptotic value of saturation fraction.

The dependence on changes in the reference environment can also be seen in the precipitation rate-instability index relationship (figure 10b); the precipitating simulations exhibit an inverse dependence of the precipitation rate on instability index, which is dependent on the reference profile. *Sentic et al.* [2015] have shown that this inverse relationship holds in observations of the Dynamics of the Madden-Julian Oscillation (DYNAMO) field campaign, which exhibited organized convection. This behavior might seem to contrasts the RCE relationship between precipitation rate and instability index (figures 2c). However, the RCE instability indices for a given SST are consistent with the relationships at that SST for a larger range of wind speeds.

The precipitation rate-GMS relationship (figure 10c), shows that the GMS approaches an asymptotic value which is SST and reference profile dependent. Notice that the asymptotic value (shown as outlined bullets) decreases from about 0.5 at 290 K SST, to about 0.2 at 310K SST. This asymptotic, or characteristic value of the GMS is a significant indicator of convective activity [*Inoue and Back*, 2015b; *Sentic et al.*, 2015]; lower characteristic values of GMS produce stronger precipitation, because of stronger import of moisture at low GMS values. Observations show that the value for this asymptotic GMS value is around 0.2 for the current climate [*Sentic et al.*, 2015].

The relationship between saturation fraction and instability index is shown for the precipitating only simulations (figure 10d); a low instability index correlates with a higher saturation fraction. The RCE relationship is also shown for each of the selected SSTs (empty colored squares), for comparison. The inverse relationship between saturation fraction and instability index is preserved for different SSTs, but the relationship depends strongly on SST; the relationship becomes more pronounced with increasing SSTs (going from the blue to the red symbols); RCE values seem to set the SST dependent shape of the relationship. Also, at higher SSTs, reference environments support a wider range of the instability indices compared to lower SSTs. At the same time, the non-precipitating simulations have much smaller values of saturation fraction over a wide range of instability index (not shown). The separation of the non-precipitating and precipitating simulations in moisture content is a feature of convective organization reported in previous research [*Bretherton et al.*, 2005; *Muller and Held*, 2012; *Wing and Emanuel*, 2013; *Coppin and Bony*, 2015].

Sentic et al. [2015] showed that observed organized convection exhibits a strong relationship between saturation fraction and GMS, and instability index and GMS (figures 10e–f); both diagnostics asymptote to an SST-dependent characteristic GMS value. The largest variations of the GMS with saturation fraction occur at lower SSTs. The non-linear behavior exhibited by the lower SST relationships is wind speed dependent; e.g. compare the 300 SST GMS behavior with saturation fraction (figure 10e) to the GMS behavior with wind speed from figure 6i, while the relationship becomes more constrained for higher SSTs. However, at all SSTs, the saturation fraction asymptotes to the characteristic value of GMS, which decreases monotonically for increasing SST and saturation fraction. A similar result holds for the relationship between instability index and GMS (figure 10f); the GMS varies strongly at low SSTs, and is more constrained for high SSTs. The characteristic value of the GMS varies non-monotonically, as a function of instability index; there is a maximum in the characteristic GMS at about 300 K SST. The instability index asymptotic value depends on the reference environment (shown in figure 9a); the reference environment might also set the asymptotic GMS value.

6. Discussion

6.1. Previous work

In this section we discuss our results and compare them qualitatively to recent research on convective organization. Research so far has focused on mechanisms responsible for formation and maintenance of convective organization in CRMs [*Bretherton et al.*, 2005; *Jeevanjee and Romps*, 2013; *Muller and Held*, 2012; *Wing and Emanuel*, 2013; *Muller and Bony*, 2015; *Bretherton and Khairoutdinov*, 2015] and GCMs [*Su et al.*, 2000; *Coppin and Bony*, 2015]. More recent studies focus on these mechanisms in a changing climate [*Coppin and Bony*, 2015; *Holloway and Woolnough*, 2016], and on the energetics of the RCE state [*Singh and O'Gorman*, 2015; *Seeley and Romps*, 2015; *Singh and O'Gorman*, 2016]. We first compare our findings to the results found in these studies, and then discuss how the precipitating and non-precipitating WTG simulations, corresponding to the precipitating and dry regions in organized convection, respectively, change in a changing climate. We then address the diagnostic relationships, how they relate to current findings, and how they change in a changing climate.

Studies investigating spontaneous convective organization in CRMs [*Bretherton et al.*, 2005; *Jeevanjee and Romps*, 2013; *Muller and Held*, 2012; *Wing and Emanuel*, 2013; *Muller and Bony*, 2015; *Bretherton and Khairoutdinov*, 2015] and GCMs [*Su et al.*, 2000; *Coppin and Bony*, 2015] have found:

1. Strong moisture gradients quantified by high saturation fraction in precipitating regions and very low values in dry regions in the organized state [*Bretherton et al.*, 2005; *Muller and Held*, 2012; *Wing and Emanuel*, 2013; *Coppin and Bony*, 2015; *Craig and Mack*, 2013], compared to the disorganized state. Our simulations exhibit similar be-

havior (figure 8e); the non-precipitating and precipitating simulations have much lower and higher values of saturation fraction, respectively, compared to the RCE saturation fraction. Note that small differences in saturation fraction correspond to large differences in the mean state of the simulations (e.g. see precipitation rate dependence on saturation fraction in figure 10a).

2. A strong influence of the longwave radiative feedbacks on development and maintenance of convective organization [*Muller and Held*, 2012; *Wing and Emanuel*, 2013; *Muller and Bony*, 2015; *Coppin and Bony*, 2015]; organized convection produces more outgoing longwave radiation compared to disorganized convection. In this study, we find similar patterns in the radiative cooling (figure 9c). Non-precipitating simulations have a stronger radiative cooling compared to the RCE, which corresponds to strong cooling in clear sky conditions in dry regions of organized convection. Precipitating simulations, on the other hand, show a decrease of radiative cooling, compared to RCE values, which decreases more with with increasing wind speeds (figure 9d).

3. The importance of surface fluxes and WISHE mechanisms for initiation and maintenance of convective organization [*Bretherton et al.*, 2005; *Wing and Emanuel*, 2013; *Muller and Bony*, 2015; *Coppin and Bony*, 2015]. While homogenizing surface fluxes hindered organization in *Bretherton et al.* [2005], *Muller and Bony* [2015] showed that larger domains could produce convective organization even with homogenized surface fluxes. In our simulations both the precipitating and non-precipitating simulations have, in general, stronger surface fluxes than the RCE surface forcing (figure 8g); previous research has also found stronger surface fluxes both in dry and precipitating regions of organized convection.

4. Up-gradient horizontal transport of moisture, which is characterized by negative GMS [*Bretherton et al.*, 2005; *Muller and Held*, 2012; *Wing and Emanuel*, 2013]. Negative GMS (figure 9g) corresponds to export of both moist entropy and moisture, and is seen in non-precipitating simulations; on the other hand, precipitating simulations have positive GMS when moisture is imported (possibly from dry regions) and entropy is exported.

Given the similarities in the qualitative behavior between multiple equilibria in precipitation and studies on convective organization, multiple equilibria in precipitation in WTG simulations are in general a useful analogy for studying convective organization. We exploit this to understand how convective organization changes with climate in the context of multiple equilibria in WTG.

Researchers have studied convective organization [*Tompkins*, 2001; *Posselt et al.*, 2012; *Wing and Emanuel*, 2013; *Emanuel et al.*, 2014; *Wing and Cronin*, 2016; *Coppin and Bony*, 2015; *Holloway and Woolnough*, 2016] and the RCE energy budget in a changing climate [*Seeley and Romps*, 2015; *Singh and O'Gorman*, 2016]. In their GCM study of the dependence of mechanisms of convective organization on SST, *Coppin and Bony* [2015] found that at low SSTs convection organized as a consequence of cold pool expansion, while at high SSTs convective organization was dominated by WISHE mechanisms. At intermediate SSTs (around 301 K), those two mechanisms played an equal role. *Posselt et al.* [2012] have shown that convective organization is influenced by the changes in the thermodynamic environment in a warming climate; they found an increase in stratiform convective activity and decrease in deep convective activity when warming from 298 K SST to 302 K SSTs in their CRM RCE simulations. This transitional behavior around 300 K SSTs has been addressed recently by *Emanuel et al.* [2014]. The authors suggested the existence of a Radiative Convective Instability (RCI) leading to convective organization dominated by cloud-radiative feedbacks, with SST the critical parameter. They showed that the RCI is fundamentally thermodynamic, dominated by water vapor, longwave radiative effects, moist convection, and large scale vertical motion through WTG effects. Several of our results support the RCI mechanism of *Emanuel et al.* [2014]. For example, our simulations suggest there is a characteristic instability index around 300 K SST; the asymptotic values of instability index (outlined bullets in figure 9a) and the multiple-to-single equilibrium transition in surface entropy fluxes have a maximum around 300 K SST (figure 8g). This characteristic behavior occurs as we change the SST and consequently the reference environment which supports the claim of *Emanuel et al.* [2014] that the RCI is of thermodynamic origin.

The phase diagram in figure 4 suggests how the thermodynamic environment might constrain mechanisms of convective organization. The region of low SSTs and lower wind speeds supports only the dry equilibrium even in moist initialized simulations. These simulations also exhibit subsidence with strong cooling at the top of the boundary layer and throughout the troposphere, similar to non-precipitating simulations from section 4.3, in contrast to cold pools produced by convective downdrafts in precipitating simulations. This behavior corresponds to the radiatively driven cold pool convective organization mechanism of *Coppin and Bony* [2015]. Our results suggest that the thermodynamic environment at low SSTs might be setting the conditions for the radiatively driven cold pool mechanism. At high SSTs, on the other hand, only multiple equilibria and a single precipitating equilibrium exist in our simulations. This can be interpreted as the thermodynamic environment supporting WISHE mechanisms more than radiative cold pool mechanisms of convective organization.

6.2. Diagnostics in the dry and precipitating state

Previous studies have hypothesized an analogy between multiple equilibria in WTG simulations, and dry and precipitating regions of organized convection [*Sobel et al.*, 2007; *Sessions et al.*, 2010; *Emanuel et al.*, 2014; *Sessions et al.*, 2015, 2016]. We next discuss the behavior of multiple equilibria in WTG simulations as a function of SST and surface wind speeds.

6.2.1. Non-precipitating simulations

The non-precipitating simulations are analogous to dry patches surrounding precipitating regions in organized convection.

We find that precipitable water, saturation fraction, surface entropy flux, instability index, radiative cooling, and DCIN are all constrained by SSTs and reference profiles in the dry state (figures 8c, 8e, 8g, 9a, 9c, 9e, respectively). While precipitable water increases for all dry simulations, saturation fraction and DCIN vary greatly for simulations close to the transition from multiple to single equilibria due to the boundary layer circulation explained in section 4.2; stronger surface fluxes lead to moistening of the lower troposphere, which in turn reduces the DCIN and produces conditions more favorable for convection. DCIN values for the simulations at the transition are much lower around 300 K SST than around 290 K and 310 K SSTs; this is a consequence of increased moistening (increased saturation fraction) which reduces the difference between surface moist entropy and saturated moist entropy above the boundary layer for intermediate SSTs. Incidentally, saturation fraction and surface entropy fluxes show a maximum around 301

K SST. The boundary layer circulation which supports this behavior in our idealized simulations was also shown to exist in other studies of convective organization [*Bretherton et al.*, 2005; *Wing and Emanuel*, 2013; *Muller and Bony*, 2015; *Sessions et al.*, 2015, 2016]. This suggests the importance of the boundary layer moistening circulation in initiation of precipitation in organized convection (see section 4).

Instability index, radiative cooling, and DCIN all vary with SST in the dry state. The instability index stays close to RCE stability values (figure 9a). The radiative cooling, on the other hand, is stronger that the RCE state (figure 9c), which is characteristic of the dry regions in organized convection; organized convection produces more OLR in the organized state [*Bretherton et al.*, 2005; *Muller and Held*, 2012; *Wing and Emanuel*, 2013; *Muller and Bony*, 2015]. The importance of the DCIN for the dry state was suggested by *Sessions et al.* [2016]; the authors found that only with interactive radiation did the non-precipitating WTG simulations exhibit strong DCIN because of strong subsidence cooling with interactive radiation. Because of the broad range DCIN exhibits in the SST-wind speed parameter space (figure 9e–f), it might be a good parameter to distinguish disorganized and organized convection in observations and simulations.

Saturation fraction, surface entropy fluxes, instability index, DCIN and GMS, all vary with wind speed in the dry simulations (figures 8f, 8h, 9b, 9f, and 9h, respectively). Both saturation fraction and surface entropy fluxes increase with wind speed (figure 8f, h), even though there is spread due to reference profile and SST variations (low SSTs have lower saturation fraction and surface fluxes). This is probably caused by the boundary layer circulation explained in section 4.1; higher wind speeds strengthen the circulation and cause moistening of the lower troposphere [*Bretherton et al.*, 2005; *Wing and Emanuel*, 2013; *Muller and Bony*, 2015]; this is supported by more negative GMS at higher wind speeds. The balance between radiatively driven subsidence and stronger surface entropy fluxes at higher wind speeds causes more negative GMS which leads to enhanced export of entropy and moisture (more moisture is exported because of higher saturation fraction).

6.2.2. Precipitating simulations

Precipitating simulations are analogous to the precipitating regions in organized convection.

Precipitation rate increases with both SSTs and wind speed (figures 8a, 8b), which suggests strengthening of organized convection in a warming environment. Since the maximum moisture content is set by the reference environment (figures 8c and 8e) the large increase in precipitation for asymptotic values of wind speeds (70 m s^{-1}) must come form surface fluxes (figures 8h), and not solely due to increased wind speeds. This happens because larger wind speeds weakly influence the maximum moisture content (figure 8d), and only make the moisture content asymptotically approach the maximum value set by the reference environment (figure 8f).

The precipitating simulations show a stark difference from non-precipitating simulations in instability index, radiative cooling, DCIN and GMS (figures 9a, 9c, 9e and 9f, and 9g and 9h, respectively). Stability of precipitating patches increases with increasing wind speed (decreasing instability index, figure 9b) but the instability index minimum is set by the reference environment (figure 9a, outlined bullets). Especially at high SSTs, the difference between the stability of dry and precipitating patches becomes larger, which implies that the instability index could be used to diagnose the strength of convective organization at higher SSTs. Interestingly, the larger the difference between the instability index between dry and precipitating simulations with SST, the smaller the spread in GMS, e.g. a 290 K SST GMS varies widely, while the instability index is rather constrained, and vice versa for 310 K SST. Since a small positive GMS corresponds to stronger convection this suggests that in a warming environment organization might become consistently stronger, while its strength can vary widely for a cooling environment. While precipitating simulations show a uniformly low to zero DCIN for all simulations (figure 9e), radiative cooling shows a weak dependence on wind speed (figure 9d), with the SST setting the minimum radiative cooling (figure 9c, outlined bullets); radiative cooling is much weaker in precipitating simulations because of increased moisture content which inhibits radiation from escaping the domain.

6.3. Diagnostic relationships in a changing climate

The relationship between precipitation and moisture has been studied both in observations [*Bretherton et al.*, 2004; *Neelin et al.*, 2009; *Peters and Neelin*, 2006; *Raymond et al.*, 2003; *Masunaga*, 2012; *Sentic et al.*, 2015] and models [*Raymond and Sessions*, 2007; *Sessions et al.*, 2015; *Sentic et al.*, 2015; *Sessions et al.*, 2016]; in general, studies have shown that the precipitation rate is a strong function of saturation fraction. We show how this relationship varies with SST and reference profiles (figure 10a inset). Increasing SSTs support higher precipitation rates for the same increase in saturation fraction; for example, an increase of 0.02 in saturation fraction at peak precipitation rates gives an increase of 50 mm d^{-1} in precipitation rate for 290 K SST, and an increase of about 200 mm d^{-1} in precipitation rate for 310 K SST. This suggests that in a warming environment the precipitating regions of organized convection may intensify. Furthermore, this relationship somewhat resembles the observational results of *Masunaga* [2012]. The author binned satellite observations of precipitation by saturation fraction and found that increasing organization (identified by higher environmental saturation fractions) lead to stronger precipitation rate-saturation fraction relationships, similar to the relationship in figure 10a inset.

The precipitation rate-instability index inverse relationship [*Raymond and Sessions*, 2007; *Sessions et al.*, 2010; *Gjorgjievska and Raymond*, 2014; *Sessions et al.*, 2015; *Sentic et al.*, 2015; *Sessions et al.*, 2016; *Raymond and Flores*, 2016] strengthens with increasing SST (figure 10b); a lower instability index produces stronger precipitation rate irrespective of SST. However, reference environments at higher SSTs exhibit this relationship much stronger, with the asymptotic value (at high surface wind speed) varying with SST (see section 5.1.2). For a given SST, a lower reference instability index makes the local convection more bottom heavy which imports moisture from lower, more moist, levels, and increases the saturation fraction, which in turn increases the precipitation rate (not shown). This relationship was recently observed in the DYNAMO field campaign [*Sentic et al.*, 2015]. The authors found a relationship in DYNAMO observations resembling the one seen in figure 10b. However, those observations were made in the current climate at SSTs around 302 K, while our simulations have been done by varying wind speeds for different SSTs and reference profiles. The relationship between precipitation rate and instability index can be possibly explained by the variation in the instability index of the reference environment in the DYNAMO observations, which is also the variable we vary by changing reference profiles in this study; however, in these simulations, at different SSTs the reference environment also changes static stability, so the proposed correspondence between this work and *Sentic et al.* [2015] might not be as clear.

The GMS quantifies convective transport between local convection and the reference environment [*Neelin and Held*, 1987; *Sobel et al.*, 2007; *Raymond et al.*, 2009; *Sessions et al.*, 2010, 2015; *Sentic et al.*, 2015; *Inoue and Back*, 2015b; *Sessions et al.*, 2016]. *Inoue and Back* [2015b] found that a characteristic GMS value separates developing convection when precipitation rates increase, and dissipating convection when precipitation rates decrease. The characteristic GMS is usually associated with peak precipitation values. GMS is small and/or negative for developing convection and smaller than the characteristic GMS value; GMS is positive and greater than the characteristic GMS value for dissipating convection. This behavior in GMS in WTG simulations has been documented in *Sessions et al.* [2010], where the authors found asymptotic behavior of the GMS approaching a characteristic value for high wind speeds. This characteristic behavior has also been seen in observations from the DYNAMO field campaign [*Sentic et al.*, 2015]. Here, we find similar behavior in the precipitating steady state (figures 10c, e, f). The steady state GMS approaches an asymptotic value for high wind speeds which we associate with the critical GMS value for high precipitation rates. We find that in a varying climate, the critical GMS value changes from about 0.5 at low SSTs, to about 0.2 at high SSTs. This change is significant because it quantifies how much the ratio between entropy export and moisture import changes in a changing climate. Small and positive GMS is associated with more intense precipitation [*Raymond et al.*, 2009; *Inoue and Back*, 2015b; *Sentic et al.*, 2015], which implies that in a warming environment, convection in precipitating regions of organized convection might get stronger. Similarly, saturation fraction increases with decreasing characteristic GMS (outlined bullets in figure 10e), while the characteristic instability index decreases for SSTs above 300 K (outlined bullets in figure 10d). A lower instability index is associated with higher saturation fraction and precipitation rates [*Gjorgjievska and Raymond*, 2014; *Sessions et al.*, 2015; *Sentic et al.*, 2015]; our results suggest that in a warming environment this relationship between instability index, saturation fraction, and precipitation rate might get stronger.

7. Summary and conclusions

In this study, we performed weak temperature gradient (WTG) simulations of multiple equilibria in precipitation at different SSTs, in order to study how convective organization might change in a changing climate. At different SSTs, we used RCE temperature and total water vapor mixing ratio profiles as reference profiles for the WTG simulations, which, depending on if the WTG domain was initialized dry or moist, exhibited a dry or precipitating steady state, or equilibrium. We assumed the hypothesized analogy between precipitating and non-precipitating WTG equilibria, and the precipitating and dry regions in organized convection. We found three regions in the SST versus wind speed phase space:

1. A region of high wind speeds with a single precipitating equilibrium, which can be interpreted as the region of less organized, scattered, convection (above the dashed line in figures 4a–b), characteristic of a disorganized state.

2. A region of intermediate wind speeds which support both a non-precipitating and a precipitating steady state (between the dashed and solid line in figures 4a–b), i.e. multiple equilibria, which can be interpreted as conditions supporting convective organization.

3. A region of low wind speeds and SSTs, which does not support convection even in a moist environment (below solid line in figures 4a–b). These conditions support strong radiatively driven cold pools, which have been shown to exist as a driving convective

organization mechanism at low SSTs [*Coppin and Bony*, 2015]. Radiatively driven cold pools exist over the whole range of SSTs in the non-precipitating simulations.

The transition between the multiple equilibria and the single precipitating equilibrium is accompanied by a boundary layer circulation which moistens the lower troposphere and leads to conditions supporting precipitation. This boundary layer circulation strengthens with increasing wind speeds and opposes the radiatively driven subsidence; these are the two opposing mechanisms controlling the onset of convective organization.

Our results support the hypothesized analogy between organized convection and multiple equilibria in WTG simulations. We found large differences in moisture content, radiative cooling, surface entropy fluxes, and large-scale transport of energy and moisture between non-precipitating and precipitating WTG simulations, all of which are characteristic of organized convection. Furthermore, previous studies suggest a characteristic, or transitional, behavior around 300 K SST which we confirm in our simulations. Around 300 K SST, the non-precipitating simulations exhibit a maximum in saturation fraction, surface entropy fluxes, and a minimum in DCIN, while precipitating simulations show a maximum in the asymptotic atmospheric stability for high wind speeds.

To study how convective organization might change in a changing climate, we diagnosed convection at different SSTs and surface wind speeds. We found the following characteristics for precipitating and non-precipitating simulations:

1. A characteristic behavior around 300 K SST for non-precipitating simulations at the transition from multiple to a single equilibrium; saturation fraction, surface entropy fluxes, and DCIN all show SST or reference environment dependence influenced by a shallow moistening circulation.

2. Increased OLR with increasing SST for non-precipitating simulations, and the opposite for precipitating simulations.

3. Strengthening precipitation with increasing SSTs, implying strengthening convection in precipitating regions of organized convection.

4. Strengthening of large-scale transport between dry and moist regions in organized convection for increasing SSTs, where organized convection is characterized by the existence of multiple equilibria, and the strength of large-scale transport is quantified by the difference in GMS between precipitating and non-precipitating WTG simulations with the same boundary conditions.

Furthermore, diagnostic relationships significant for convective organization suggest:

1. A strengthening of the relationship between precipitation rate and saturation fraction at higher SSTs, which shows increases in saturation fraction, and consequently precipitation rate, for higher SSTs.

2. A stronger relationship between instability index and precipitation rate, and saturation fraction and instability index in a warming environment (increasing SSTs). The precipitating WTG equilibrium shows decreasing instability index with increasing SST. Previous WTG simulations showed that decreasing instability index concentrates moisture convergence at low levels which increases saturation fraction and precipitation rate. This is in contrast with the instability behavior in the RCE state; the RCE instability index increases for increasing SST.

3. Differences in the large-scale transport between non-precipitating and precipitating simulations also increase in a warming environment. The characteristic GMS value, which quantifies the strength of large-scale circulations, decreases with increasing SSTs, which

indicates stronger export of entropy and import of moisture. The change in the characteristic GMS value is reflected in the diagnostic relationships between GMS and precipitation rate, instability index, and saturation fraction. All of these relationships were shown to play a role in organized convection.

In conclusion, our results suggest similarities between the precipitating and the non-precipitating WTG multiple equilibria simulations, and precipitating and dry regions in organized convection, and that it can be used to study how convective organization changes in a changing climate. Further, we show the usefulness of convective diagnostics such as instability index, saturation fraction, and GMS, and their relationships, as measures of convective organization in a changing climate.

Acknowledgments. We thank David Raymond, Michael Herman, Patrick Haertel, and Larissa Back for fruitful discussions. We would like to acknowledge high-performance computing support from Yellowstone (ark:/85065/d7wd3xhc) provided by NCAR's Computational and Information Systems Laboratory, sponsored by the National Science Foundation. The model data used in this study can be obtained by contacting the corresponding author (stipo.sentic@student.nmt.edu). This work was supported by U. S. National Science Foundation Grants ATM-0352639, ATM-1021049, ATM-1342001, AGS-1056254, and AGS-1342001.

References

Anber, U., S. Wang, and A. Sobel (2014), Response of atmospheric convection to vertical wind shear: Cloud-system-resolving simulations with parameterized large-scale circulation. part i: Specified radiative cooling, *J. Atmos. Sci.*, *71*, 2976–2993, doi:10.1175/JAS-

D-13-0320.1.

Anber, U., S. Wang, and A. Sobel (2015), Effect of surface fluxes versus radiative cooling on tropical deep convection, *J. Atmos. Sci.*, *72*, 3378–3388, doi:10.1175/JAS-D-14-0253.1.

Bretherton, C. S., and M. F. Khairoutdinov (2015), Convective self-aggregation feedbacks in near-global cloud-resolving simulations of an aquaplanet, *Journal of Advances in Modeling Earth Systems*, *7*(4), 1765–1787, doi:10.1002/2015MS000499.

Bretherton, C. S., and P. K. Smolarkiewicz (1989), Gravity waves, compensating subsidence and detrainment around cumulus clouds, *J. Atmos. Sci.*, *46*, 740–759.

Bretherton, C. S., M. E. Peters, and L. E. Back (2004), Relationships between water vapor path and precipitation over the tropical oceans, *Journal of Climate*, *17*(7), 1517–1528.

Bretherton, C. S., P. N. Blossey, and M. Khairoutdivnov (2005), An energy-balance analysis of deep convective self-aggregation above uniform sst, *J. Atmos. Sci.*, *62*, 4273–4292, doi:10.1175/JAS3614.1.

Coppin, D., and S. Bony (2015), Physical mechanisms controlling the initiation of convective self-aggregation in a general circulation model, *Journal of Advances in Modeling Earth Systems*, *7*(4), 2060–2078.

Craig, G. C., and J. M. Mack (2013), A coarsening model for self-organization of tropical convection, *Journal of Geophysical Research: Atmospheres*, *118*(16), 8761–8769, doi:10.1002/jgrd.50674.

Daleu, C. L., S. J. Woolnough, R. S. Plant, D. J. Raymond, S. L. Sessions, A. H. Sobel, G. Bellon, S. Wang, A. Cheng, M. J. Herman, P. Peyrille, P. Siebesma, and D. Kim (2015), Intercomparison of methods of coupling between convection and large-scale circulation: I. comparison over uniform surface conditions, *J. Adv. Model. Earth Syst.*, doi:doi:10.1002/2015MS000468, in press.

Emanuel, K., A. A. Wing, and E. M. Vincent (2014), Radiative-convective instability, *Journal of Advances in Modeling Earth Systems*, *6*(1), 75–90.

Feng, Z., S. Hagos, A. K. Rowe, C. D. Burleyson, M. N. Martini, and S. P. de Szoeke (2015), Mechanisms of convective cloud organization by cold pools over tropical warm ocean during the amie/dynamo field campaign, *Journal of Advances in Modeling Earth Systems*, *7*(2), 357–381, doi:10.1002/2014MS000384.

Gjorgjievska, S., and D. J. Raymond (2014), Interaction between dynamics and thermodynamics during tropical cyclogenesis, *Atmos. Chem. Phys.*, *14*, 3065–3082, doi:10.5194/acp-14-3065-2014.

Herman, M. J., and D. J. Raymond (2014), WTG cloud modeling with spectral decomposition of heating, *J. Adv. Model. Earth Syst.*, *6*, 1121–1140, doi:10.1002/2014MS000359.

Holloway, C. E., and S. J. Woolnough (2016), The sensitivity of convective aggregation to diabatic processes in idealized radiative-convective equilibrium simulations, *Journal of Advances in Modeling Earth Systems*, *8*(1), 166–195, doi:10.1002/2015MS000511.

Inoue, K., and L. Back (2015a), Gross moist stability assessment during TOGA COARE: Various interpretations of gross moist stability, *J. Atmos. Sci.*, doi:10.1175/JAS-D-15-0092.1, in press.

Inoue, K., and L. E. Back (2015b), Gross moist stability assessment during toga coare: Various interpretations of gross moist stability, *Journal of the Atmospheric Sciences*, *72*(11), 4148–4166.

Jeevanjee, N., and D. M. Romps (2013), Convective self-aggregation, cold pools, and domain size, *Geophys. Res. Lett.*, *40*, 1–5, doi:10.1002/grl.50204.

Khairoutdinov, M., and K. Emanuel (2013), Rotating radiative-convective equilibrium simulated by a cloud-resolving model, *Journal of Advances in Modeling Earth Systems*, *5*(4), 816–825.

Masunaga, H. (2012), Short-term versus climatological relationship between precipitation and tropospheric humidity, *J. Climate*, *25*, 7983–7990, doi:10.1175/JCLI-D-12-00037.1.

Mlawer, E., S. Taubman, P. Brown, M. Iacono, and S. Clough (1997), Rrtm, a validated correlated-k model for the longwave, *J. Geophys. Res.*, *102*(16), 663–682.

Muller, C., and S. Bony (2015), What favors convective aggregation, and why?, *Geophys. Res. Let.*, *42*, 5626–5634.

Muller, C. J., and I. M. Held (2012), Detailed investigation of the self-aggregation of convection in cloud-resolving simulations, *J. Atmos. Sci.*, *69*, 2551–2565, doi:10.1175/JAS-D-11-0257.1.

Neelin, J. D., and I. M. Held (1987), Modeling tropical convergence based on the moist static energy budget, *Mon. Weat. Rev.*, *115*, 3–12, doi:10.1175/1520-0493(1987)115<0003:MTCBOT>2.0.CO;2.

Neelin, J. D., O. Peters, and K. Hales (2009), The transition to strong convection, *Journal of the Atmospheric Sciences*, *66*(8), 2367–2384.

Peters, O., and J. D. Neelin (2006), Critical phenomena in atmospheric precipitation, *Nat. Phys.*, *2*, 393–396, doi:10.1038/nphys314.

Posselt, D. J., S. v. d. Heever, G. Stephens, and M. R. Igel (2012), Changes in the interaction between tropical convection, radiation, and the large-scale circulation in a warming environment, *Journal of Climate*, *25*(2), 557–571.

Raymond, D. J. (2001), A new model of the madden-julian oscillation, *J. Atmos. Sci.*, *58*(18), 2807–2819, doi:10.1175/1520-0469(2001)058<2807:ANMOTM>2.0.CO;2.

Raymond, D. J. (2007), Thermodynamic control of tropical rainfall, *Quarterly Journal of the Royal Meteorological Society*, *126*(564), 889–898, doi:10.1002/qj.49712656406.

Raymond, D. J., and M. M. Flores (2016), Predicting convective rainfall over tropical oceans from environmental conditions, *J. Adv. Model. Earth Syst.*, doi: 10.1002/2015MS000595.

Raymond, D. J., and S. L. Sessions (2007), Evolution of convection during tropical cyclogenesis, *Geophys. Res. Lett.*, *34*, L06,811, doi:10.1029/2006GL028607.

Raymond, D. J., and X. Zeng (2005), Modelling tropical atmospheric convection in the context of the weak temperature gradient approximation, *Q. J. Roy. Meteor. Soc.*, *131*, 1301–1320, doi:10.1256/qj.03.97.

Raymond, D. J., G. B. Raga, C. S. Bretherton, J. Molinari, C. López-Carrillo, and Ž. Fuchs (2003), Convective forcing in the intertropical convergence zone of the eastern Pacific, *J. Atmos. Sci.*, *60*, 2064–2082.

Raymond, D. J., S. L. Sessions, and Z. Fuchs (2007), A theory for the spinup of tropical depressions, *Q. J. Roy. Meteor. Soc.*, *133*, 1743–1754, doi:10.1002/qj.125.

Raymond, D. J., S. L. Sessions, A. H. Sobel, and Z. Fuchs (2009), The mechanics of gross moist stability, *J. Adv. Model. Earth Syst.*, *1*, 9, doi:10.3894/JAMES.2009.1.9.

Raymond, D. J., S. Gjorgjievska, S. L. Sessions, and Z. Fuchs (2014), Tropical cyclogenesis and mid-level vorticity, *Austral. Meteor. Ocean. J.*, *64*, 11–25.

Schreck III, C. J. (2015), Kelvin waves and tropical cyclogenesis: A global survey, *Monthly Weather Review*, *143*(10), 3996–4011.

Seeley, J. T., and D. M. Romps (2015), Why does tropical convective available potential energy (cape) increase with warming?, *Geophysical Research Letters*, *42*(23), 10,429–10,437, doi:10.1002/2015GL066199, 2015GL066199.

Sentic, S., S. L. Sessions, and Željka Fuchs (2015), Diagnosing convection with weak temperature gradient simulations of DYNAMO, *J. Adv. Model. Earth Syst.*, doi: 10.1002/2015MS000531.

Sessions, S. L., S. Sugaya, D. J. Raymond, and A. H. Sobel (2010), Multiple equilibria in a cloud resolving model using the weak temperature gradient approximation, *J. Geophys. Res.*, *115*, D12110, doi:10.1029/2009JD013376.

Sessions, S. L., M. J. Herman, and S. Sentic (2015), Convective response to changes in the thermodynamic environment in idealized weak temperature gradient simulations, *J. Adv. Model. Earth Sys.*, *7*, 712–738, doi:10.1002/2015MS000446.

Sessions, S. L., S. Sentic, and M. J. Herman (2016), The role of radiation in organizing convection in weak temperature gradient simulations, *J. Adv. Model. Earth Syst.*, doi: 10.1002/2015MS000587.

Singh, M. S., and P. A. O'Gorman (2015), Increases in moist-convective updraught velocities with warming in radiative-convective equilibrium, *Quarterly Journal of the Royal Meteorological Society*, *141*(692), 2828–2838, doi:10.1002/qj.2567.

Singh, M. S., and P. A. O'Gorman (2016), Scaling of the entropy budget with surface temperature in radiative-convective equilibrium, *Journal of Advances in Modeling Earth Systems*, pp. n/a–n/a, doi:10.1002/2016MS000673.

Sobel, A., S. Wang, and D. Kim (2014), Moist static energy budget of the MJO during DYNAMO, *J. Atmos. Sci.*, *71*(11), 4276–4291, doi:10.1175/JAS-D-14-0052.1.

Sobel, A. H., and C. S. Bretherton (2000), Modeling tropical precipitation in a single column, *J. Climate*, *13*, 4378–4392, doi:10.1175/1520-0442(2000)013<4378:MTPIAS>2.0.CO;2.

Sobel, A. H., G. Bellon, and J. Bacmeister (2007), Multiple equilibria in a single-column model of the tropical atmosphere, *Geophys. Res. Lett.*, *34*, L22,804, doi: 10.1029/2007GL031320.

Su, H., C. Bretherton, and S. Chen (2000), Self-aggregation and large-scale control of tropical deep convection: a modeling study, *J. Atmos. Sci.*, *57*, 1797–1816.

Thorncroft, C., and K. Hodges (2001), African easterly wave variability and its relationship to atlantic tropical cyclone activity, *Journal of Climate*, *14*(6), 1166–1179.

Tobin, I., S. Bony, and R. Roca (2012), Observational evidence for relationships between the degree of aggregation of deep convection, water vapor, surface fluxes, and radiation, *Journal of Climate*, *25*(20), 6885–6904.

Tompkins, A. M. (2001), On the relationship between tropical convection and sea surface temperature, *Journal of Climate*, *14*(5), 633–637, doi:10.1175/1520-0442(2001)014<0633:OTRBTC>2.0.CO;2.

Wang, S., and A. H. Sobel (2011), Response of convection to relative sea surface temperature: cloud-resolving simulations in two and three dimensions, *J. Geophys. Res.*, *116*, D11,119, doi:10.1029/2010JD015347.

Wang, S., and A. H. Sobel (2012), Impact of imposed drying on deep convection in a cloud-resolving model, *J. Geophys. Res.*, *117*, D02112, doi:10.1029/2011JD016847.

Wang, S., A. H. Sobel, and Z. Kuang (2013), Cloud-resolving simulation of TOGA-COARE using parameterized large-scale dynamics, *J. Geophys. Res. Atmos.*, *118*(12), 6290–6301, doi:10.1002/jgrd.50510.

Wang, S., A. H. Sobel, A. Fridlind, Z. Feng, J. M. Comstock, P. Minnis, and M. L. Nordeen (2015), Simulations of cloud-radiation interaction using large-scale forcing derived from the cindy/dynamo northern sounding array, *Journal of Advances in Modeling Earth Systems*, *7*(3), 1472–1498.

Wing, A. A., and T. W. Cronin (2016), Self-aggregation of convection in long channel geometry, *Quarterly Journal of the Royal Meteorological Society*, *142*(694), 1–15, doi:10.1002/qj.2628.

Wing, A. A., and K. A. Emanuel (2013), Physical mechanisms controlling self-aggregation of convection in idealized numerical modeling simulations, *J. Adv. Mod. Earth Sys.*, *5*, 1–14, doi:10.1002/2013MS000269.

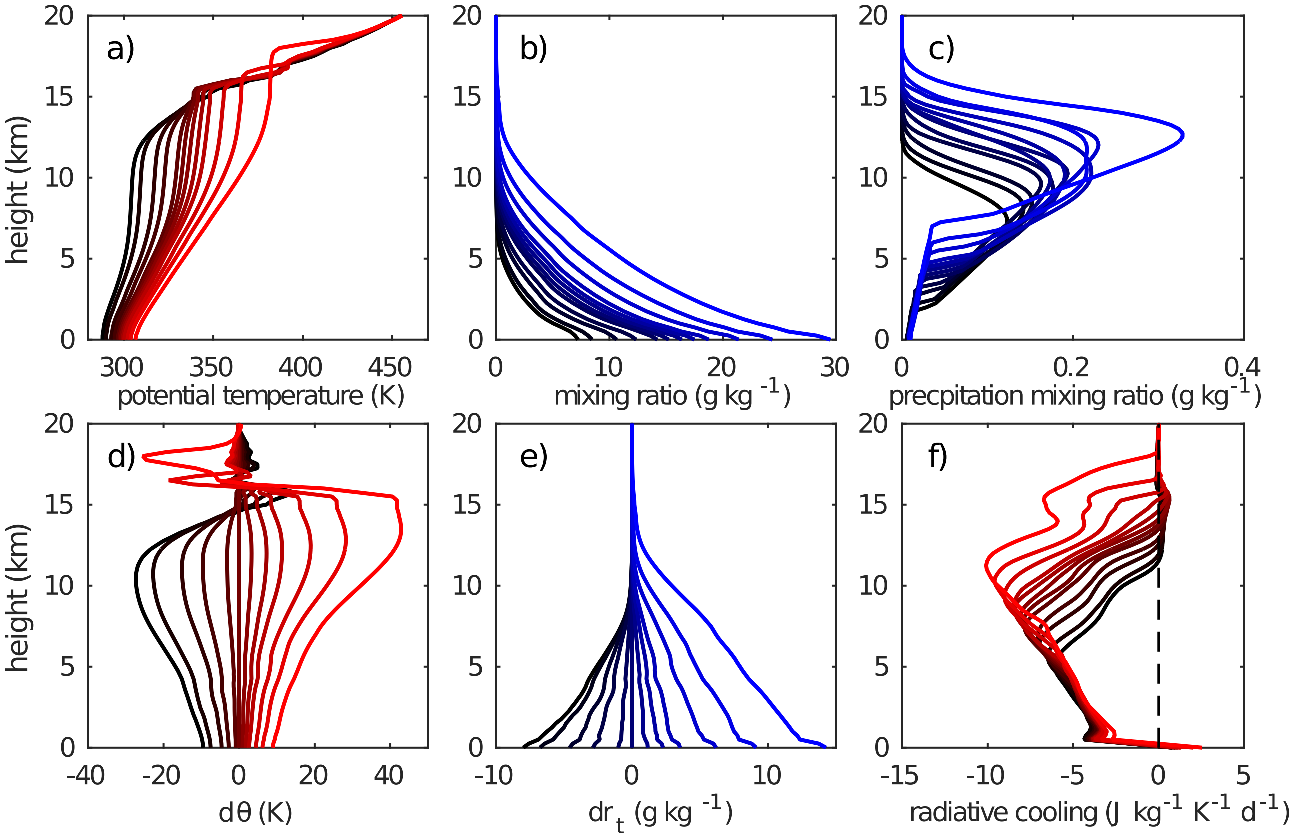

Figure 1. Radiative convective equilibrium (RCE) profiles of (a) potential temperature, (b) mixing ratio, (c) precipitation mixing ratio, (d) potential temperature anomaly relative to the 300 K SST reference profile, (e) mixing ratio anomaly relative to the 300 K SST reference profile, and (f) radiative cooling, for reference SSTs ranging from 290 K (black line) to 310 K (red or blue line). Warmer SSTs produce a warmer and moister RCE environment compared to cool SSTs, while radiative cooling (f) balances the convective activity (c) in the radiative convective equilibrium (RCE) state. Profiles in panels (a) and (b) are used as reference profiles in WTG simulations. For visual distinction, temperature related variables are plotted in red shades, while moisture related variables are plotted in blue shades.

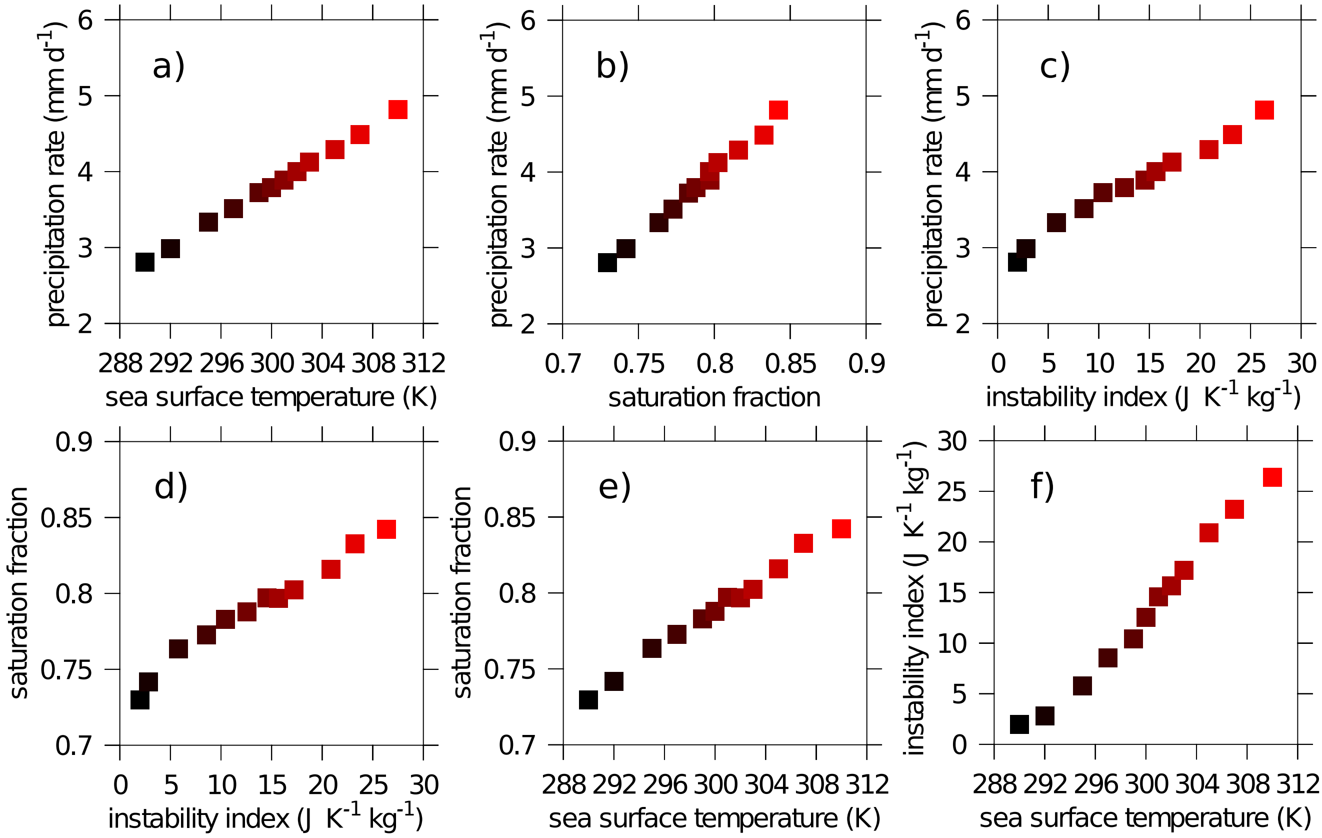

Figure 2. RCE diagnostic relationships between precipitation rate and (a) SSTs, (b) saturation fraction, and (c) instability index, and (d) saturation fraction and instability index, and (e) saturation fraction and SST, and (f) instability index and SST.

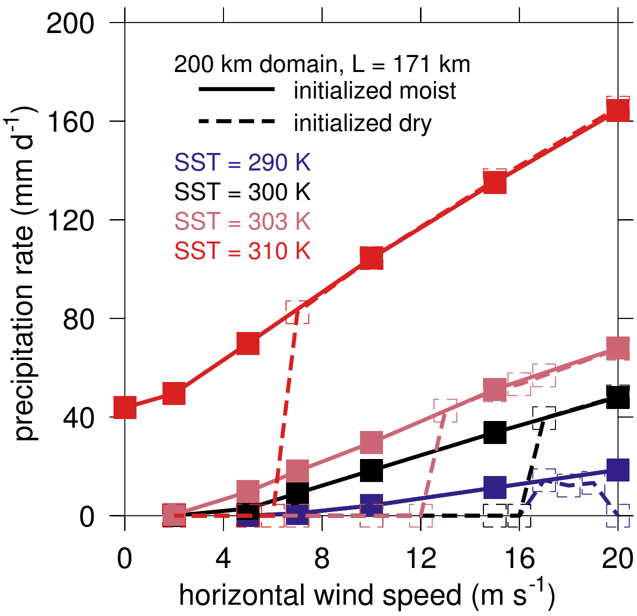

Figure 3. Precipitation rate versus horizontal wind speed for weak temperature gradient (WTG) simulations at different SSTs. For each SST we use RCE profiles of potential temperature and mixing ratio as the reference profiles at the same SST, but we either initialize the simulation dry (dashed line, empty symbols) or moist (solid line, solid symbols). Regions of multiple equilibria are defined as the range of wind speeds supporting both a dry and a precipitating state, e.g. 3 to 12 m s^{-1} for 303 K SST; wind speeds lower than 3 m s^{-1} and higher than 12 m s^{-1} support a single dry and moist equilibrium, respectively. Note that the wind speed at which the single dry equilibrium goes to multiple equilibria, and the wind speed from which the multiple equilibria go to a single precipitating equilibrium, change with SST. Also, the precipitation rate increases with increasing SST and horizontal wind speed.

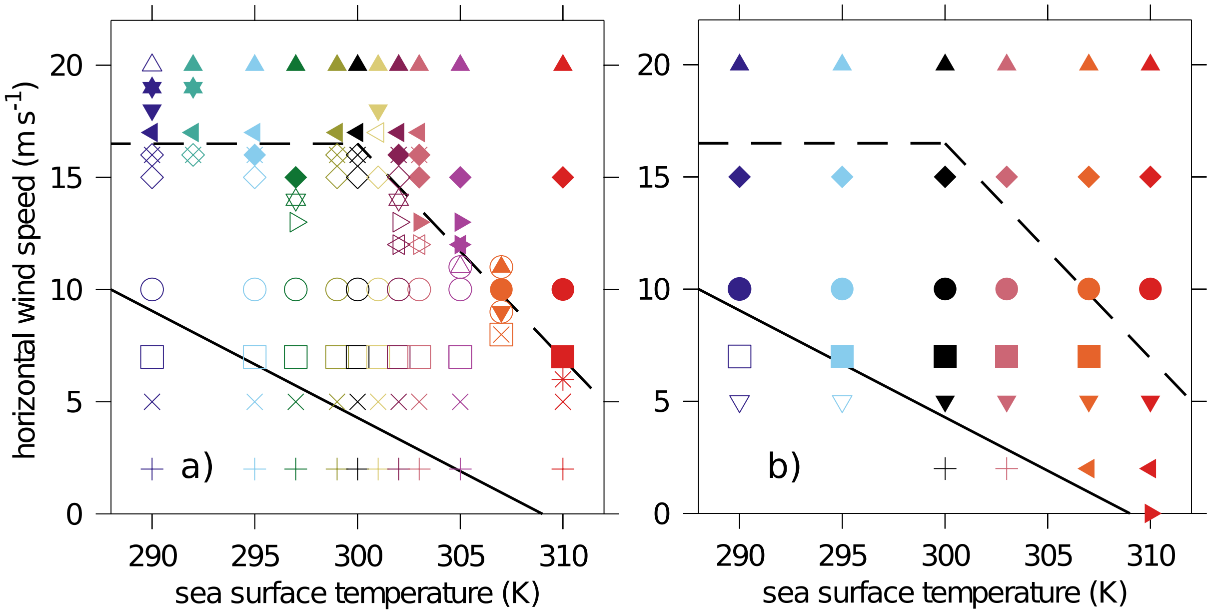

Figure 4. Precipitating (solid symbols) and non-precipitating (empty symbols) simulations as a function of SST and horizontal wind speed, for a (a) dry, and (b) moist initialization. Different colors correspond to different SSTs, while different symbols correspond to different wind speeds. The dashed and solid lines are eye-guides separating three regions: below the solid line exists a single non-precipitating equilibrium, between the solid and the dashed lines is a region of multiple equilibria in precipitation, while above the dashed line exists a single precipitating equilibrium. NOTE: This plot serves as the symbol and color legend for figures 7, 8, 9, and 10.

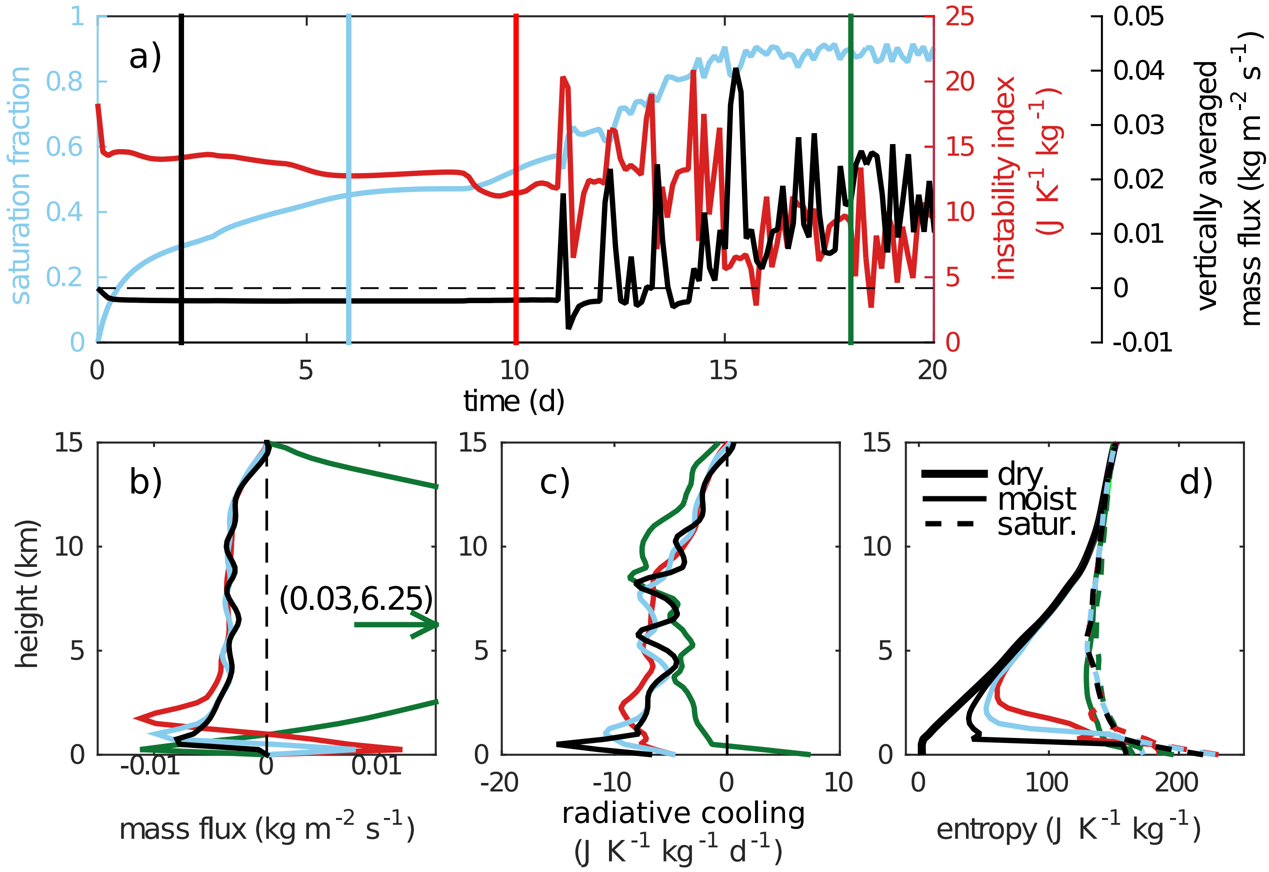

Figure 5. (a) Time series of saturation fraction, instability index, and vertically averaged mass flux, and vertical profiles of (b) mass flux, (c) radiative cooling, and (d) entropy, for a precipitating simulation at 303 K SST, and 13 m s^{-1} wind speed. The vertical lines in (a) represent times (2, 7, 10, and 18 days) at which vertical profiles are plotted in b, c, and d. Colors correspond to time in days.

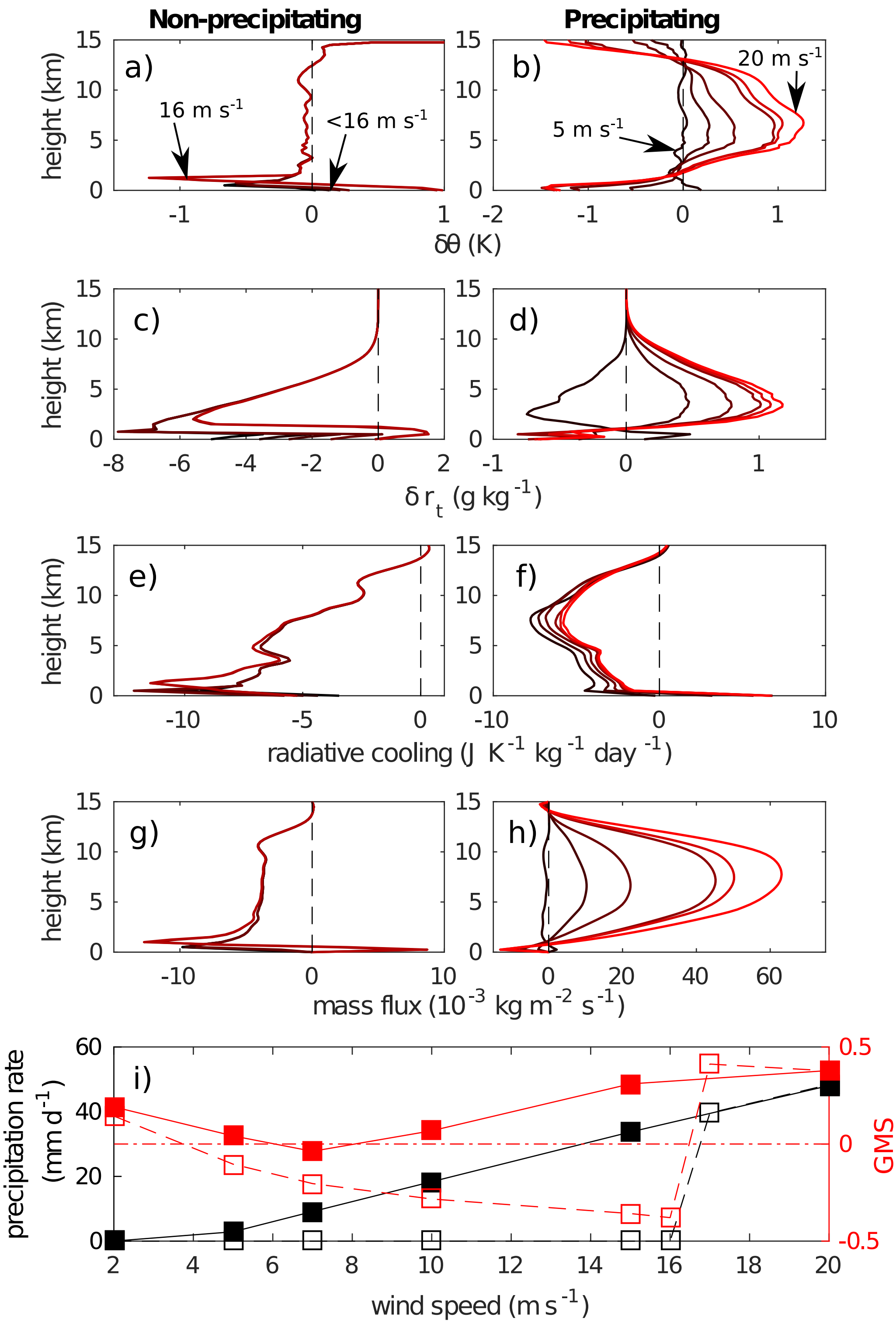
Non-precipitating
Precipitating
a)
b)
c)
d)
e)
f)
g)
h)
i)
16 m s-1
<16 m s-1
20 m s-1
5 m s-1
height (km)
δθ (K)
δ r t (g kg -1)
radiative cooling (J K -1 kg -1 day -1)
mass flux (10 -3 kg m -2 s -1)
precipitation rate (mm d -1)
GMS
wind speed (m s -1)

Figure 6.

Figure 6. (continued)

Vertical profiles of: (a–b) the potential temperature anomaly from the reference profile, (c–d) the total water vapor mixing ratio anomaly from the reference profile, (e–f) the radiative cooling, and (g–h) the mass flux; for non-precipitating simulations on the left (a, c, e, and g), and precipitating simulations on the right (b, d, f, and h), and (i) precipitation rate (black) and GMS (red) versus wind speed, at the 300 K SST. In panels a–h, the shade indicates increasing wind speed from 2 m s^{-1} (black) to 20 m s^{-1} (red).

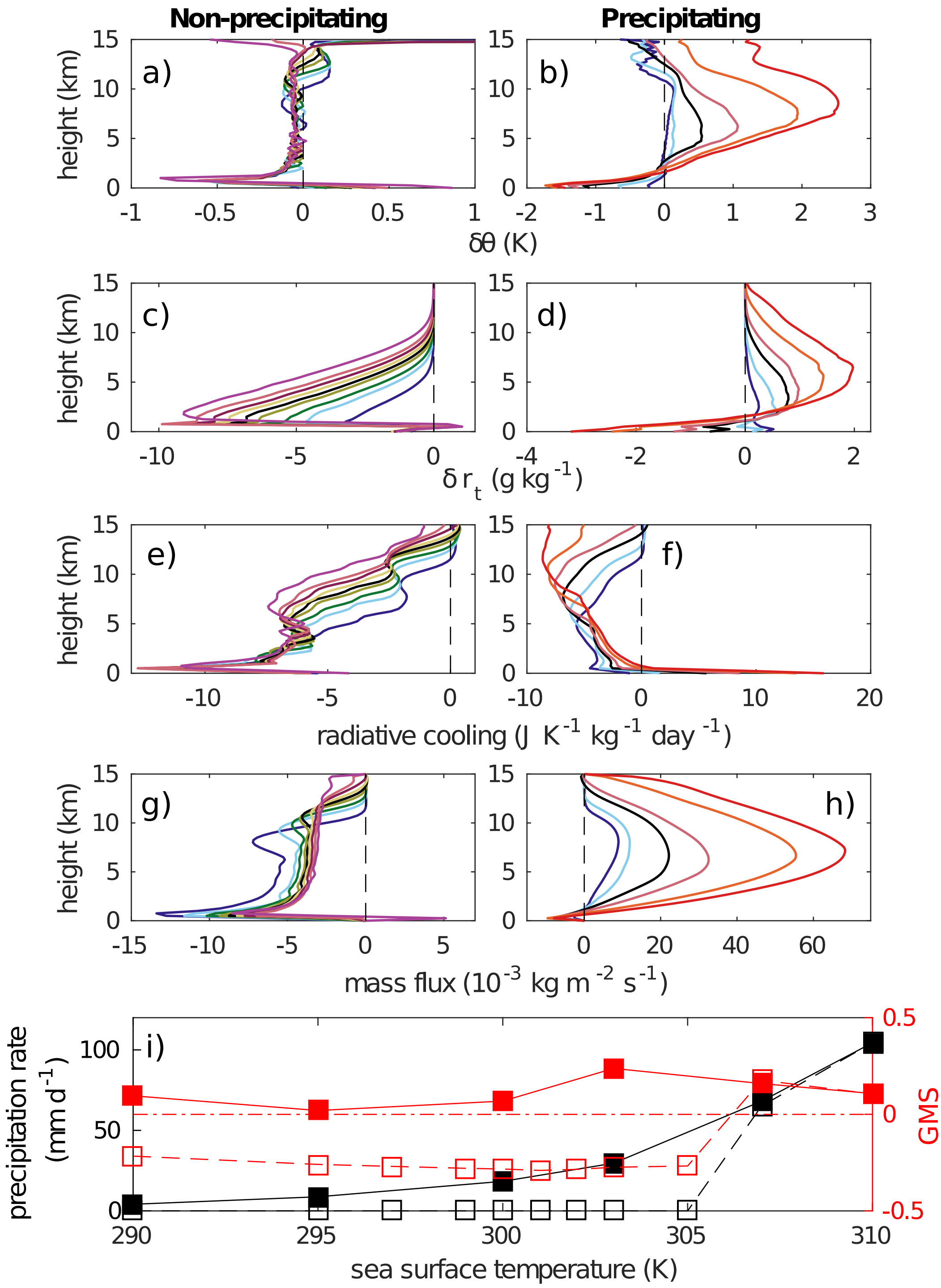

Non-precipitating
Precipitating
a)
b)
c)
d)
e)
f)
g)
h)
i)
height (km)
δθ (K)
δ r_t (g kg^-1)
radiative cooling (J K^-1 kg^-1 day^-1)
mass flux (10^-3 kg m^-2 s^-1)
precipitation rate (mm d^-1)
GMS
sea surface temperature (K)

Figure 7.

Figure 7. (continued)

Vertical profiles of: (a–b) the potential temperature anomaly from the reference profile, (c–d) the total water vapor mixing ratio anomaly from the reference profile, (e–f) the radiative cooling, and (g–h) the mass flux; for non-precipitating simulations on the left (a, c, e, and g), and precipitating simulations on the right (b, d, f, and h), and (i) precipitation rate (black) and GMS (red) versus SST, at 10 m s^{-1} wind speed. Color indicates different SSTs (see figure 4 for color legend).

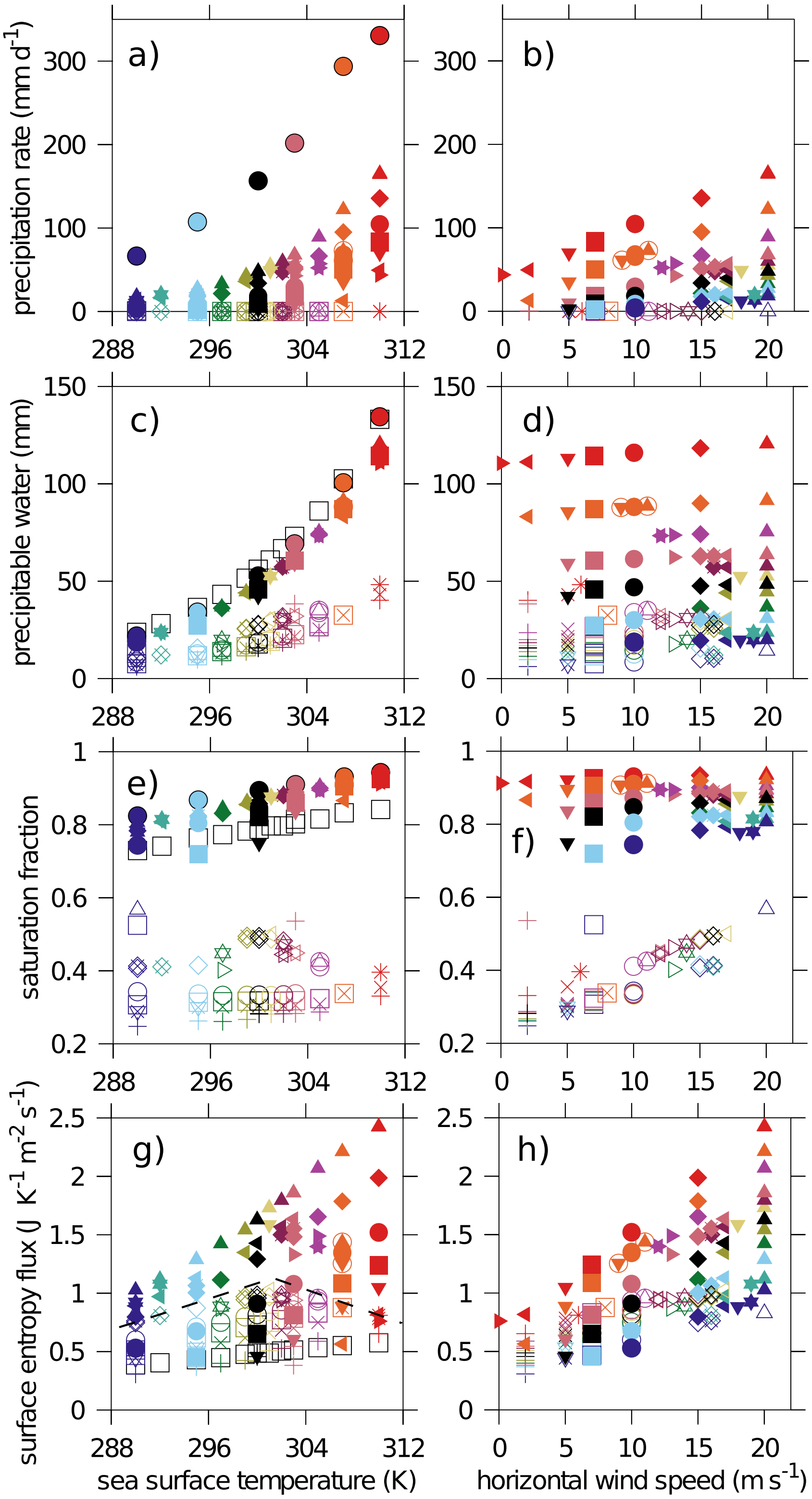
a)
b)
c)
d)
e)
f)
g)
h)
precipitation rate (mm d^{-1})
precipitable water (mm)
saturation fraction
surface entropy flux (J K^{-1} m^{-2} s^{-1})
sea surface temperature (K)
horizontal wind speed (m s^{-1})
288
296
304
312
0
5
10
15
20

Figure 8.

Figure 8. (continued)

(a–b) Precipitation rate, (c–d) precipitable water, (e–f) saturation fraction, and (g–h) surface entropy flux, versus SSTs (a, c, e, and g) and horizontal wind speed (b, d, g, and h). Figure 4 serves as the legend for symbol shapes and colors. Outlined filled bullets correspond to simulations with 70 m s^{-1} wind speed. Panels c, e and g also show RCE values of precipitable water, saturation fraction, and surface entropy fluxes, respectively (empty black squares).

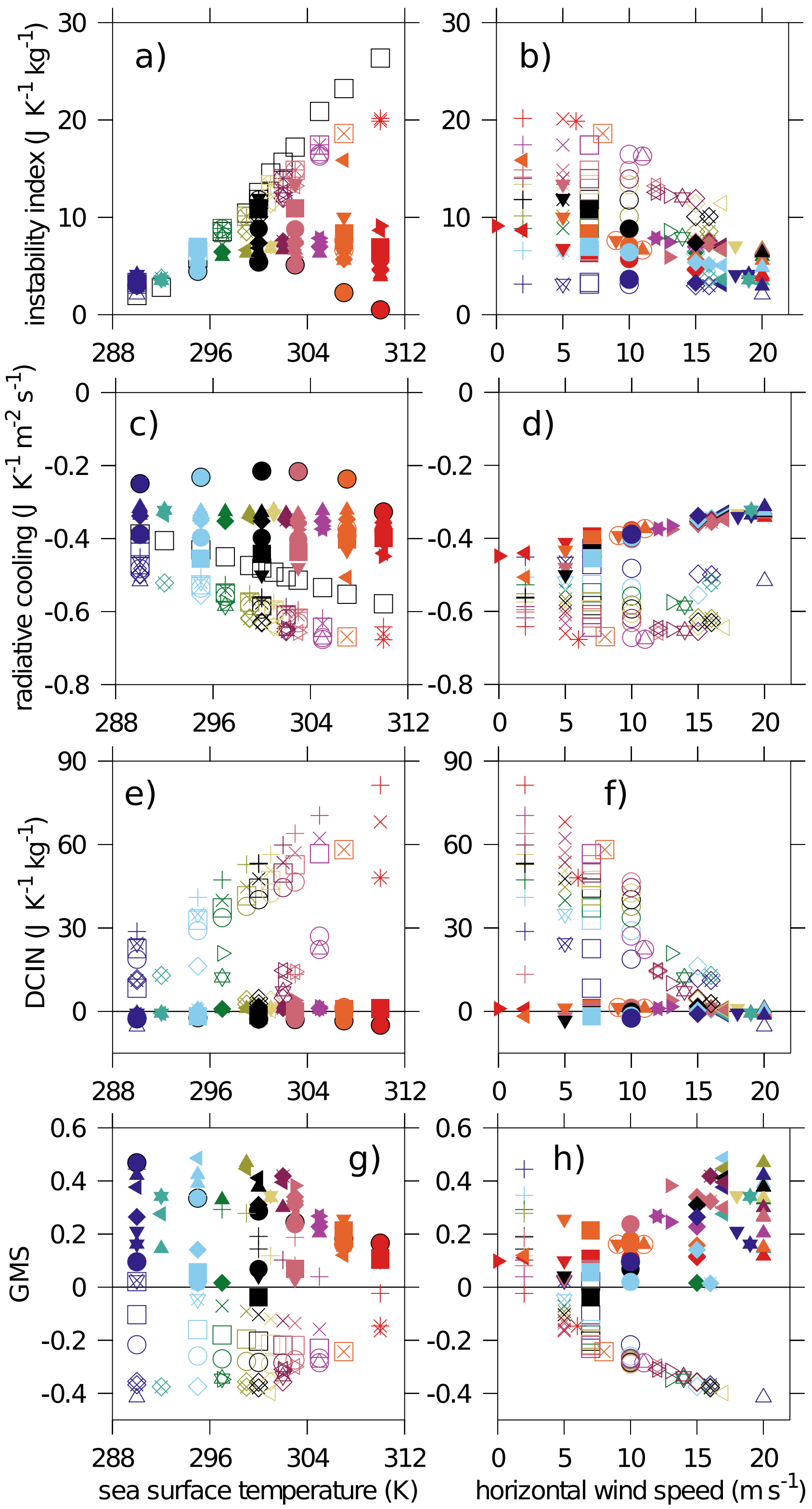
a)
b)
c)
d)
e)
f)
g)
h)
instability index (J K-1 kg-1)
radiative cooling (J K-1 m-2 s-1)
DCIN (J K-1 kg-1)
GMS
sea surface temperature (K)
horizontal wind speed (m s-1)
288
296
304
312
0
5
10
15
20
30
20
10
0
-0.2
-0.4
-0.6
-0.8
90
60
0.6
0.4
0.2
-0.2
-0.4

Figure 9.

Figure 9. (continued)

(a–b) Instability index, (c–d) radiative cooling, (e–f) DCIN, and (g–h) GMS, versus SSTs (a, c, e, and g) and horizontal wind speed (b, d, g, and h). Figure 4 serves as the legend for symbol shapes and colors. Outlined filled bullets correspond to simulations with 70 m s^{-1} wind speed. Panels a and c also show RCE values of instability index, and radiative cooling (empty black squares).

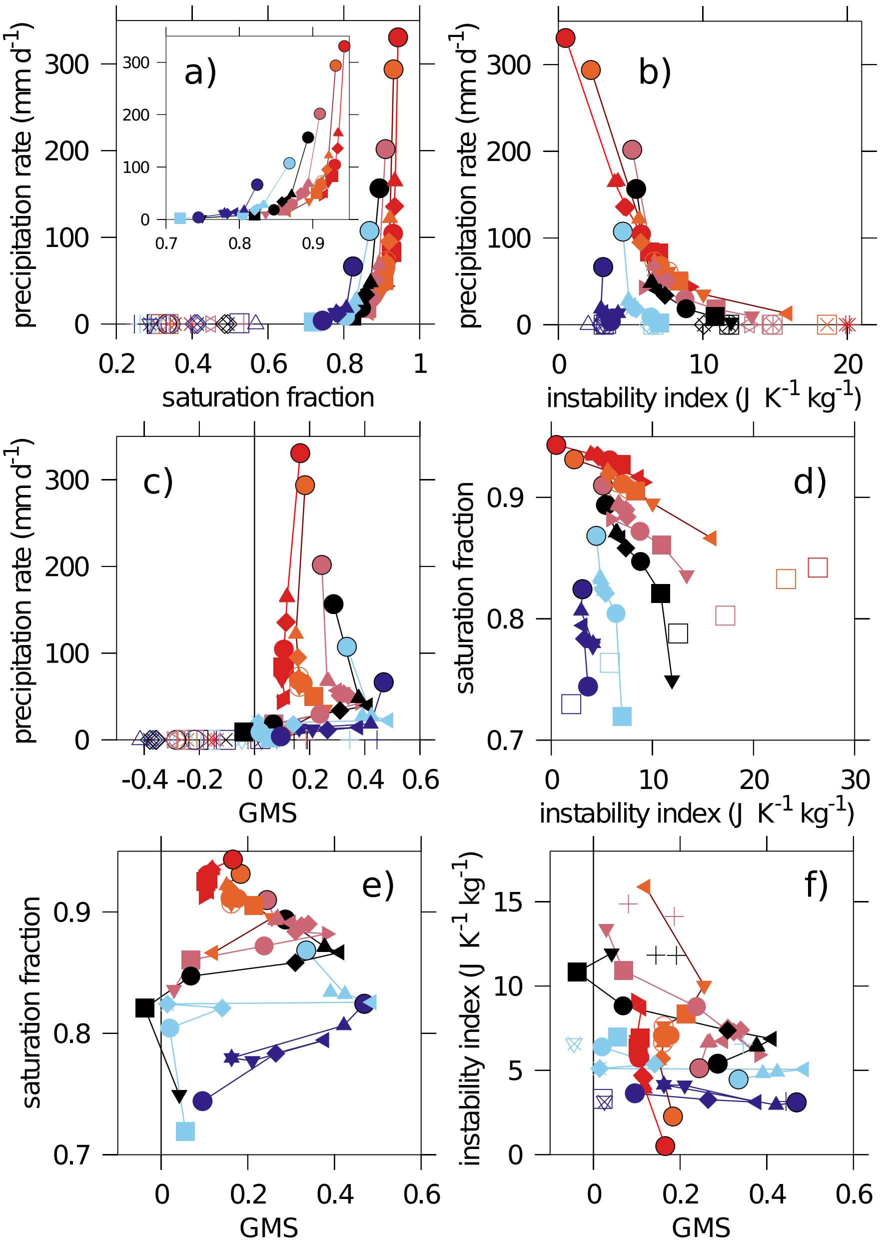

Figure 10. Precipitation rate versus (a) saturation fraction, (b) instability index, and (c) GMS; saturation fraction versus (d) instability index, and (e) GMS; and (f) instability index versus GMS. Panel a show an insets which magnifies the relationship for the precipitating simulations, while panels d–f focus on the precipitating simulations, with panel d also showing RCE values with empty squares. Figure 4 serves as the legend for symbol shapes and colors.